Master's thesis

NTNU
Norwegian University of Science and Technology
Faculty of Engineering
Department of Mechanical and Industrial Engineering

Valeria Usenco

ANN Analysis of DOFS Measurements Compromised by Mechanical and Acoustic Vibrations

Master's thesis in Mechanical Engineering
Supervisor: Kaspar Lasn
June 2022

NTNU
Norwegian University of
Science and Technology

Valeria Usenco

ANN Analysis of DOFS Measurements Compromised by Mechanical and Acoustic Vibrations

Master's thesis in Mechanical Engineering
Supervisor: Kaspar Lasn
June 2022

Norwegian University of Science and Technology
Faculty of Engineering
Department of Mechanical and Industrial Engineering

NTNU
Kunnskap for en bedre verden

Abstract

Distributed optical fibre sensors (DOFSs) are becoming increasingly popular for in-situ condition monitoring in traditional engineering applications. DOFSs can also be deployed for new, innovative applications such as monitoring currents in the ocean. The main advantage of using DOFSs is that they can provide high-resolution continuous strain and temperature measurements over long distances. However, the measurements are sensitive to ambient disturbances such as mechanical and acoustic vibrations, which produce high levels of noise. How ambient vibrational noise affects the strain data is unclear and is investigated in this thesis. To this end, artificial neural networks (ANNs) are employed to classify distinct mechanical and acoustic disturbances. Gaining a better understanding of measurement noise and how numerical tools can be used to classify it is an important step in securing the use of DOFSs for novel applications.

This investigation involves a series of physical experiments employing bare free-hanging DOFSs and a DOFS bonded to a beam. First, using free-hanging fibres, raw amplitude data from the DOFSs is analysed to investigate the extent of the fibre-end reflection. It is established that approximately 150 mm of the fibre end is affected by the end-reflection, with large variations between different physical optical fibres. Thereafter, the bare DOFSs are subjected to a series of magnitude-controlled mechanical disturbances. The strain pattern is visually different depending on the source and intensity of the disturbance. Two disturbance classification algorithms are developed using long short-term memory (LSTM) ANNs and temporal convolution networks (TCNs). The algorithms reach prediction accuracies of over 70% for regular and ca. 90% for composite disturbance states. Parametric studies confirm that the prediction capability is robust regarding the sensing resolution but highly dependent on the training data quantity.

In the final experiment, a DOFS is fixed to a long composite beam subjected to near-eigenfrequency acoustic disturbances. When exposed to tones close to the first eigenfrequency of the beam, spikes appear in the strain measurements corresponding to the location of the antinode in the expected mode shape. To classify the frequency class, two TCNs are developed: one where each frequency is treated as an individual class (categorical predictions) and one where the frequency is tied to a single output neuron (continuous predictions). Both networks identify the correct frequencies to some degree, with the categorical TCN performing better than the continuous TCN. The findings of the parametric study concerning the training data set size agree with the previous study.

The experiments and data analyses presented in this thesis provide a better understanding of DOFS noise effects from mechanical and acoustic disturbances. The numerical analysis demonstrates how LSTM ANNs and TCNs can be used for the classification of DOFS data. This is an advancement in extracting new information from noisy DOFS measurements.

Sammendrag

Distribuerte optisk-fiber sensorer (DOFS) blir stadig oftere anvendt til kontinuerlig situasjonsovervåkning av strukturer. Ny forskning har også undersøkt nye og innovative bruksområder til eksisterende nettverk med DOFS, f.eks. havstrømsovervåkning med undersjøiske kabler. Hovedfordelen med DOFS sammenlignet med andre sensorer er at de kan måle tøyning (eller temperatur) kontinuerlig over lange distanser og med høy oppløsning. DOFS blir lett påvirket av mekaniske og akustiske vibrasjoner fra omgivelsene som fører til mye støy i distribuerte tøyningsmålinger. Kunstige nevrale nett (ANN) blir brukt til å klassifisere distinkte akustiske og mekaniske forstyrrelser. En økt forståelse av støy i DOFS-målinger og hvordan numeriske verktøy kan brukes til klassifisering er et viktig og nødvendig steg mot å sikre framtidstidsrettet bruk av DOFS.

Arbeidet er bygd opp av flere eksperimentelle forsøk med bare, fritthengende fibre og en fiber festet til en struktur. I det første forsøket brukes det amplitudemålinger til å etablere hvor langt enderefleksjonen propagerer i fiberen. Det blir fastslått at ca. de siste 150 mm av fiberen blir påvirket av enderefleksjonen, men det er store variasjoner blant fibrene som blir testet. Deretter utsettes bare, fritthengende fibre for kontrollerte mekaniske forstyrrelser. Tøyningsmålinger blir visuelt annerledes avhengig av kilden og intensiteten til forstyrrelsen. Det blir utviklet to ANN-modeller til å klassifisere forstyrrelser i målingene: et tidskonvolusjonsnettverk (TCN) og et langtidskorttidsminnenettverk (LSTM). Begge klarer å klassifisere seks distinkte dataklasser med over 70% presisjon og tre samensatte dataklasser med over 90% presisjon. Etterfølgende parametriske studier viser at metoden er lite avhengig av prosesseringsparameterne, men svært avhengig av mengden treningsdata.

I det siste forsøket blir en fiber festet til en lang komposittbjelke utsatt for akustiske forstyrrelser i ulike frekvenser. Når den akustiske frekvensen er ca. bjelkens egenfrekvens blir det observert høye tøyningsverdier i antinoden til den første forventede bøyningsmodusen. To TCN blir utviklet til å klassifisere frekvensene: ett hvor frekvensen behandles som én kontinuerlig klasse og ett hvor hver frekvens behandles som en egen kategorisk klasse. Begge nettverk klarer å klassifisere frekvensen til en viss grad. Det kategoriske nettverket gir det beste resultatet. De parametriske studiene samsvarer med studiene fra det forrige forsøket.

Forsøkene gir en bedre forståelse av støy i DOFS målinger som oppstår fra mekaniske og akustiske forstyrrelser. De numeriske analysene viser hvordan DOFS data kan klassifiseres med LSTM og TCN. Konseptet markerer et skritt mot å kunne ekstrahere ny informasjon fra målinger påvirket av støy.

Автореферат

Распределённые волоконные световодные датчики (РВСД) приобретают всё большую популярность при локальном мониторинге состояния конструкций. В новейших исследованиях рассматривается возможность применения ранее реализованных оптических волокон в качестве РВСД в инновационных областях, например, для мониторинга океанических течений. Самое большое преимущество РВСД состоит в том, что они позволяют осуществлять квазинепрерывные замеры растяжения и температуры с высоком разрешением на большом протяжении по всей длине световода. Однако, они чрезмерно чувствительны к пертурбациям окружающей среды, например к акустическим и механическим вибрациям, приводящим к высокому уровню шума при распределённых измерениях растяжения. Каким именно образом окружающий шум влияет на данные по растяжению составляет предмет настоящего исследования. Для этого рассматривается концепция применения искусственных нейронных сетей (ИНС) для классификации отдельных механических и акустических помех.

Исследование основано на ряде экспериментов, в которых применяются голые свободноподвешенные световоды, а также световоды, прикрепленные к жесткой конструкции. В первом эксперименте анализируются первичные данные по амплитуде, получаемые от РВСД при помощи свободноподвешенных волокон. Результаты показывают, что воздействие концевого отражения распространяется примерно до 150 мм от конца световода. Во втором эксперименте голые свободноподвешенные световоды подвергаются ряду механических воздействий с контролируемой интенсивностью. Анализ данных показывает, что картина растяжения меняется в зависимости от источника и интенсивности помех. Разработаны алгоритмы классификации помех на основе ИНС с долгой краткосрочной памятью (ДКСП) и темпоральных свёрточных сетей (ТСС). Алгоритмы обеспечивают точность прогноза свыше 70% по шести различным состояниям помех и около 90% для состояний с составным – высоким и низким уровнем помех. Параметрические исследования подтверждают, что точность прогноза существенно не зависит от чувствительности разрешения в измеряемых данных, но во многом зависит от количества обучающих данных.

В третьем эксперименте один РВСД был приклеен к длинной рейке из композитного материала, на которую воздействовали периодическими акустическими пертурбациями, близкими к частоте собственных колебаний рейки. При воздействии тоном с частотой в интервале в несколько герц относительно собственной частоты рейки измерения показывали скачки растяжения, соответствующие локализации пучности при первом режиме изгибных колебаний. С целью классификации частот были разработаны две ТСС: одна, где каждая частота выделена в отдельный класс (категориальный прогноз); другая, где частота привязана к отдельному нейрону с непрерывным прогнозом. Обе сети способны в определенной мере правильно определять частоту, однако категориальная ТСС показала себя лучше, чем непрерывная. Выводы параметрического исследования относительно размера набора обучающих данных согласуются с данными предшествующего исследования.

Указанные эксперименты обеспечивают лучшее понимание шума со статистической точки зрения и показывают возможность выводить новую информацию из данных по РВСД анализом на основе ТСС и ИНС с ДКСП.

Preface

This thesis marks the end of my 5-year master's degree in Mechanical Engineering. Even though I chose this degree, I have always been interested in computer science as well. Luckily, I have had the opportunity to cultivate my interest in computer science by taking courses in deep learning, machine learning, and programming. Therefore, it seemed natural to write a master's thesis involving these topics in a mechanical engineering application.

This piece of work really reflects my technical interests as it has allowed me to combine elements from different engineering disciplines. I have also learned that sensing with optical fibres is an exciting topic with a lot of unexplored areas, so I am glad to have been able to contribute with research in this field. On a final note, an abstract is provided in Russian as it is my mother tongue alongside English.

Trondheim, 02.06.2022
Valeria Usenco

Acknowledgements

Firstly, I would like to say a huge thank you to my supervisor, Kaspar Lasn, for always being supportive, motivating and dedicating so much time to my work. After our weekly meetings I was never short of ideas or in doubt of what to do next. Thank you!

Next, a big thank you to Shaoquan Wang for introducing me to the OBR device and giving me ideas at the start of the project. Thank you, Håkon Bakke, for your support with the practical work. I would also like to acknowledge Victor Maneval, for showing me how to make a laminate and Børge Holen, for cutting up the laminate.

Finally, I would like to thank my family and friends. Thank you, mum and dad, for being the best role models and always supporting me. An extra thank you goes out to my dad for helping me write the abstract in Russian. Thank you, Oliwia, for always keeping my hopes up and thank you, Kirill, for answering all my maths questions for as long as I can remember.

Table of Contents

List of Figures

List of Tables

List of Acronyms

AE absolute error. 50

ANN artificial neural network. viii, ix, 1–5, 16, 17, 19, 21, 23, 25, 26, 30, 34, 36–38, 40–42, 50, 53

CNN convolutional neural network. 24, 27

CV coefficient of variation. 31, 33

DOFS distributed optical fibre sensor. viii, ix, 1–10, 12–14, 26, 27, 30–34, 36, 41, 44, 46, 47, 51, 53

ECDF empirical cumulative distribution function. 23

FC/APC ferrule connector/angle physical contact. viii, 7, 9

FCNN fully-connected neural network. 3

FFT fast Fourier transform. viii, 29, 37, 41, 45, 51

FOS fibre optic switch. 6, 12

FRP fibre-reinforced plastic. 2

GADF Gramian angular difference field. viii, 28, 35, 36, 40, 41, 46

GAF Gramian angular field. 18, 27

GASF Gramian angular summation field. 28

GL gauge length. 7, 35, 42

LSTM long short-term memory. viii, 3, 4, 16, 23, 24, 26, 34, 37–39, 41–43, 53

MA moving average. ix, 30–33

MAE mean absolute error. ix, 23, 50, 52

ML machine learning. 2, 3, 13, 16, 21

OBR optical backscatter reflectometry. viii, 4–8, 12, 14, 17, 30, 41, 51

OF optical fibre. 1, 2, 5, 9, 12, 30, 31, 33, 34, 36, 37, 40, 44, 51, 53

OFDR optical frequency domain reflectometry. 6

PDF probability density function. 35, 37, 45

PSU power supply unit. 10

PWM pulse width modulation. 10

RMSE root mean squared error. 34

RNN recurrent neural network. 23, 24

SHM structural health monitoring. 1

SS sensor spacing. 7, 35, 42

SVM support vector machine. 3

TCN temporal convolutional network. 4, 16, 24, 26, 34, 38, 39, 41–44, 47, 49, 50, 52, 53

1 Introduction

Distributed optical fibre sensors (DOFSs) are advanced sensors which are increasingly used for structural health monitoring (SHM) due to their unique sensing characteristics. DOFS can produce high-resolution quasi-continuous strain or temperature data along the whole length of the optical fibre. However, DOFS measurements have been observed to suffer from noise due to ambient disturbances, such as mechanical or acoustic vibrations. The noise is often unwanted and renders a measurement invalid. Being able to interpret the noise effectively could make the noisy measurements useful. This thesis is centred on gaining a better understanding of the vibrational noise effects using artificial neural networks (ANNs).

1.1 Background

1.1.1 Distributed Optical Fibre Sensors

Distributed optical fibre sensors (DOFSs) are a subset of optical fibres (OFs) which are used for distributed strain or temperature measurements. DOFS can sense changes along the whole length of the fibre. This is analogous to placing thousands of overlapping strain gauges on a structure. Due to their non-intrusiveness and versatility, DOFSs have a large number of applications. For structural integrity monitoring, DOFSs are an excellent choice. Table 1.1 provides a concise overview of the useful characteristics of DOFS and which applications draw benefit from them. These examples are taken from real-life uses found in literature and demonstrate the large variety of suitable applications for DOFSs.

As the sensor core is made of glass, DOFSs are resilient to harsh environments. Although the glass core of the fibre is brittle, DOFSs can be integrated to closely follow structural geometries due to the surrounding layer of coating. The small diameter of the fibre makes it an almost non-intrusive sensing option to be integrated into tight spaces and offers a high resolution-to-sensor-weight ratio. DOFSs serve both as a sensor and the signal carrier which means no extra wires are necessary. Furthermore, since the communication medium is light, the DOFSs are immune to electromagnetic interference, removing a significant security threat which wireless sensors are often exposed to [1].

Table 1.1: Examples of DOFS characteristics and applications

Characteristic	Applications/Benefits	Ref.
Resistant to electromagnetic interference	Less vulnerable to cyber-attacks	[1]
Resistant to aggressive chemicals	Nuclear reactors	[2]
Weather-resistant	Exposed structures, geotechnical applications	[3]
Resistant to corrosion	Marine environments	[4]
Low weight per sensor	High-performance, “smart" materials	[5]
Small and non-intrusive	Between material layers in additive manufacturing, ropes, FRP laminates	[3, 4, 6]
No extra wires necessary	Less intrusion when embedded in structures	[6]
Quasi-continuous monitoring with high precision	Long-distance monitoring and error localisation, e.g. pipeline integrity monitoring	[7]

A steadily growing field of DOFS applications is in fibre-reinforced plastics (FRPs) where DOFS have several advantages over traditional metal strain gauges. The thermal expansion coefficient of OF is closer to that of a typical FRP in comparison to traditional strain gauges [4]. Furthermore, OFs are small in diameter, making them significantly less intrusive that strain gauges. DOFSs can be embedded in additively manufactured structures without any external adhesives, in contrast to strain gauges. The list of applications of DOFSs is constantly expanding as they are being applied in new and innovative ways. For example, a recent BBC News article discussed the possibility of utilising DOFSs to detect earthquakes and monitor ocean currents using the 1.3 million km grid of underwater internet cables [8]. Thus, being able to interpret DOFS signals affected by vibrations is a highly contemporary and relevant research topic.

1.1.2 Artificial Neural Networks

ANNs are a versatile computational tool which can be adapted to almost any problem ranging from image classification to prediction of sales. The availability and quality of data are central aspects of ANN deployment. Therefore, the ability to generate large amounts of data quickly makes DOFSs a good pairing with ANNs. In supervised learning, an ANN is trained to recognise patterns in data (by optimising the parameters) which can match the input to the correct output of the problem. The main mechanism in training a network is penalising for incorrect predictions by using a loss function and propagating the error penalty through the network in order to adjust the parameters accordingly. The steps in training an ANN have been described previously as part of the project thesis [9]. Contrary to traditional machine

learning (ML) methods, deep ANNs do not require prior feature extraction, as the network extracts the relevant features by adjusting the network parameters accordingly. This makes ANNs an excellent choice for problems where the relationship between the input and output of the system/model is not immediately apparent.

Applying machine learning on DOFSs data is an emerging topic. Li et al. [10] performed an extensive review of pattern recognition methods used with DOFSs. The review identified ca. twenty published examples of ML applied on DOFS data in the context of vibration sensing over long distances. The most relevant literature examples are summarised in Table 1.2. Several studies have successfully used ANNs to classify strain data. Only one study applied an ANN on strain data gathered using the same method used in this thesis, but the data was not used for classification purposes. The studies also used a variety of ANN structures, including one which used an LSTM-based structure, which suggests that the choice of ANN structure is flexible.

Table 1.2: Applications of ML on DOFS data

Application	ML Methods Used	Ref.
Damage detection and localisation for pipeline monitoring	Convolutional LSTM FCNN, 4-layer FCNN	[11, 12]
Estimating deformation from strain results calculated using OBR technology	FCNN with 3 layers	[13]
Perimeter security using amplitude data	*ResNet50*, *VGG16*	[14, 15]
Dynamic strain measurements in aerospace composite structures	Support vector machine (SVM)	[16]
Removing noise from multimode fibre temperature measurements affected by mechanical disturbances	Deep ANN with 6 layers	[17]

1.2 Problem Description

Despite the numerous sensing possibilities with DOFSs, they have a few limitations. The high sensitivity of DOFSs can lead to unwanted effects on the measurements. External mechanical vibrations and acoustic disturbances often cause measurements to be noisy. The reason behind this phenomenon is poorly understood, which limits the use of the DOFSs. Furthermore, the noisy data may hold patterns and new information not immediately obvious to the human eye.

Developing a method which can detect and classify noisy environments can expand the possibilities of DOFS used for monitoring. The overall aim of the thesis is to understand the relationships between the nature of the disturbance and the noise produced in the DOFS strain measurement. Specifically, the classification of different vibrational disturbances (both regular and chaotic) is performed. The strain data is investigated and clarified using statistical analyses and ANNs.

1.3 Scope

DOFSs are complex sensors with data generation capabilities based on the specific measurement principle. The experiments in this study are carried out using the optical backscatter reflectometry (OBR) equipment based on the Rayleigh backscattering phenomenon. The data collected will be limited to quasi-continuous arrays of strain measurements and it does not cover point-wise or temperature measurements.

For the classification tasks, two existing ANN structures (LSTM and TCN) are modified using hyperparameters. The chosen ANN structures are commonly used for time series data. Given the sequential nature of DOFS data, it can be treated similarly to a time series as there is no principal difference between sequential data arrays.

1.4 Structure

A thorough analysis of noise in DOFS data is undertaken in this thesis, approaching the topic from several perspectives. As such, the experimental work increases in complexity in three increments.

1. First, a purely statistical analysis of raw amplitude free-hanging DOFS data establishes how much data should be discarded from the end of the DOFS measurement due to interference from the tip-termination end-reflection. Throughout the rest of the work, the established end-reflection length is discarded from the DOFS measurements.

2. Then, both statistical and ANN analyses are employed on free-hanging DOFS data exposed to controlled mechanical disturbances. These analyses are used as a starting point for the disturbance classification method due to the simplicity of the test setup. Furthermore, the effect of the external vibrations on the DOFS data is presumed to be most prominent in bare DOFSs.

3. Finally, a DOFS is bonded to a beam structure. This experiment tests the ANN classification method in a more realistic and practical use case. This is a more complex scenario and interference is expected from the physical structure in the form of stabilisation and damping of the DOFS movements.

The contents of the thesis are divided into four chapters. The introduction gives a broad overview of the topic in the context of scientific literature and formulates the research problem. The setups of three different experiments are jointly explained in the “Materials and Methods” chapter due to similarities amongst them. The OBR measurement procedure is described, accompanied by examples from the measurement software. The main data processing procedures are introduced. The steps required to build an ANN model are described and the neural network structures such as LSTM and TCN are presented.

The results analysis and discussion for each experiment are presented separately in the “Experimental Results” chapter. This chapter is divided into three main sections corresponding each investigation. Each section concludes with a discussion of the results.

The final chapter provides a concise summary of the main insights from all the experimental work and reiterates the most important takeaways from each experiment. An overall conclusion is stated for the application of ANNs on DOFS measurements compromised by mechanical and acoustic vibrations.

2 Materials and Methods

This chapter begins with an introduction to DOFS and the OBR measurement principle. Then, the specifics of the OBR measurement procedure are described step-by-step. Furthermore, test setups, procedures and relevant equations for the experimental work are introduced. The final section of the chapter introduces machine learning algorithms, code structure, definitions and procedures for building an ANN.

2.1 Distributed Optical Fibre Sensing

2.1.1 Optical Fibres

A single OF is made up of a glass core with a high refractive index surrounded by a different glass cladding which has a lower refractive index. This structure causes total internal reflection to occur, allowing light to travel along the core of the fibre. The core and the cladding are coated by a thin layer of protective material (a polyamide coating in this case) which can be further encased in a rubber jacket to protect the fibre. Single-mode fibres have one thin core, which carries a single wave of light. Together with the cladding and coating, a typical single-mode OF has a total diameter of approximately 160 µm. Fibres which are used for distributed strain or temperature measurements are referred to as distributed optical fibre sensors (DOFSs). A single-mode polymer-coated OF (SMB-E1550H) from *OFS Optics* has been used as the DOFS medium in this experimental work. The main specifications are summarised in Table 2.1.

Table 2.1: DOFS specifications adapted from [18]

Characteristic	**Value**
Core diameter	6.5 µm
Cladding diameter	125 ± 2 µm
Coating diameter	155 ± 15 µm
Operating wavelength	1550 nm
Attenuation	≤ 0.7 dB/km
Operating temperature	-65 to 300 °C
Short-term bend radius	≥ 10 mm
Long-term bend radius	≥ 17 mm

2.1.2 Measurement Principle (Optical Backscatter Reflectometry)

The refractive index of the fibre has random fluctuations due to microscopic variations in the fibre material. This causes some light to be naturally scattered while it is travelling through the core. This is

referred to as Rayleigh scattering when the variations in the glass are smaller than the wavelength of light. The procedure of interpreting the backwards scattering of the light is referred to as optical backscatter reflectometry (OBR). More specifically, the OBR technology used in the experimental work is in the category of optical frequency domain reflectometry (OFDR) as it is performed in the frequency domain. When the fibre is exposed to changes in strain or temperature, the backscatter signal changes. Using OBR to interpret the difference in backscatter before and after the external change allows for the strain and/or temperature to be extracted. Hence two readings are needed to get a strain/temperature measurement: one which is used as the reference (baseline), and one after the perturbation is applied.

2.1.3 Measurement Procedure

All DOFS measurements in this thesis are conducted at constant room temperature, so any temperature effects on the measurement and corresponding signal analysis effects are hereby intentionally discarded.

The process of taking a strain measurement can be divided into two steps: the recording stage and the post-processing stage. *Luna Innovations OBR v13* software is used in the recording stage to physically send pulses of light through the fibre and save the OBR data in a binary file which is only legible for a machine with bespoke software. The light is sent by a tunable laser source and received back by the fibre optic switch (FOS) to which the fibres are connected. The *Luna Innovations FOS v1* programme is used to select which channel (out of eight) to read the signal from. A measurement takes approximately 3-4 s to perform. To take many measurements, a Python script can be used to scan and save files automatically. Python scripts use UI-automation to move the mouse cursor to the correct positions.

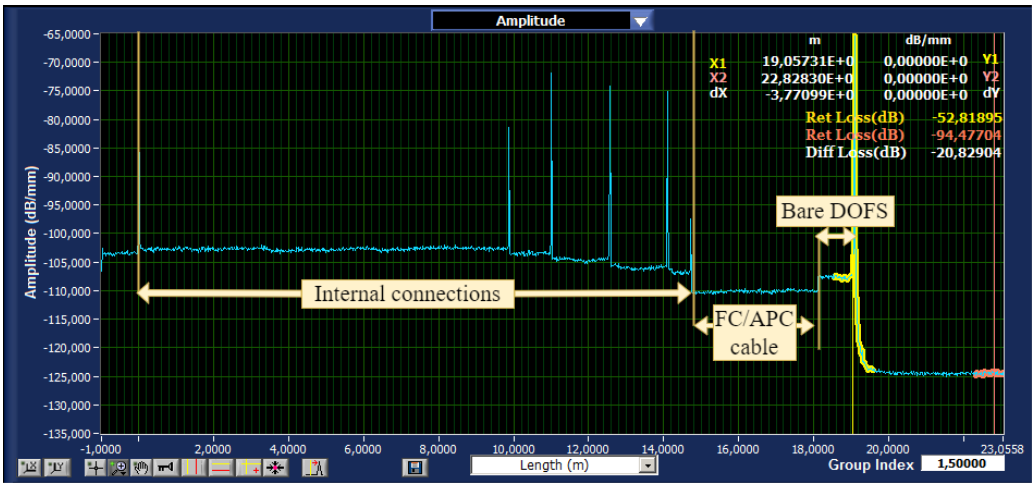

Figure 2.1: Amplitude curve from the OBR measurement

Figure 2.1 shows a typical loss amplitude curve from an OBR measurement which appears in the *Luna Innovations OBR v13* programme after taking a measurement. While the light travels through the fibre, the signal becomes weaker due to light scattering and absorption. The loss amplitude is a measure of signal attenuation or how much weaker the signal becomes. The first 14.1113 ± 0.00911 m of the total measurement length is made up of internal connections within the OBR device. The next section of the curve is the first part of the measurement fibre which is encased in a rubber jacket for protection and

connected to a ferrule connector/angle physical contact (FC/APC). Only the last labelled part of the curve is the bare DOFS as described in Table 2.1. It can be inferred that the bare DOFS has a higher intrinsic signal attenuation than the jacketed connector part. Sharp increases in loss amplitude can be observed as localised peaks along the amplitude curve. This occurs every time there is a fused splice connection between two fibres that were previously separate.

2.1.4 Post-Processing Procedure

The raw binary files have to be post-processed into text format strain data by using the *Luna Innovations OBR Desktop v3* software. The most important features of this software are highlighted in Figure 2.2. The first step in the post-processing procedure is to determine the total length of the fibre. This can be done by pressing the "find peak" button until the vertical cursor is positioned at the end-reflection peak and reading off the position. The yellow portion of the graph is the sensing selected range (symmetrically surrounding the vertical cursor), which is the segment of data to be extracted into text format.

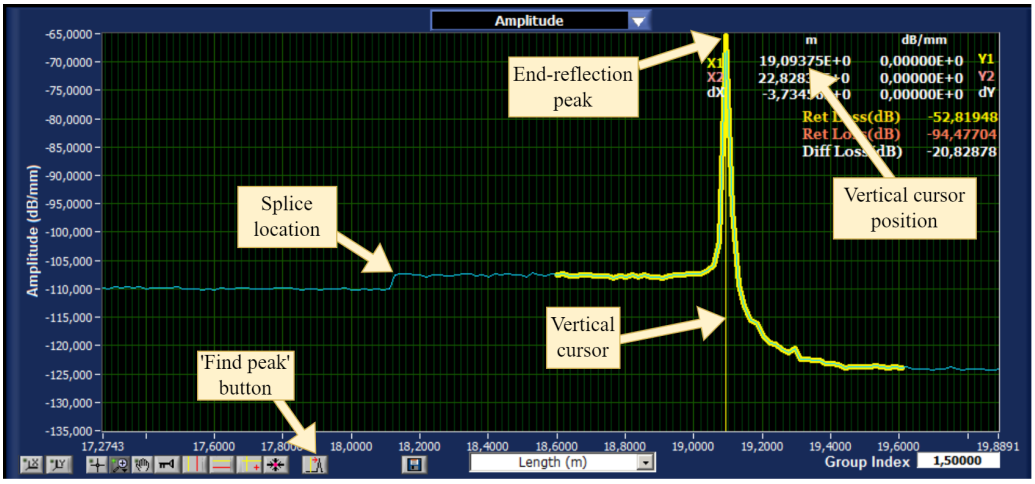

Figure 2.2: Main features of the *Luna Innovations OBR v13* desktop programme

Python scripts can also be used in the post-processing stage to automatically calculate strains in text format by using UI-automation of the *Luna Innovations OBR Desktop v3* software. The user can manually choose which measurements to save in a text file. This includes primary data such as signal amplitude and other signal characteristics. With the sensing option enabled, secondary (i.e. post-processed) data such as strain and temperature can be saved for a given set of sensing parameters. To generate text data from primary measurements, only one OBR file is needed. Two files are needed to measure strain or temperature: a reference file and a measurement file. The strain/temperature is calculated based on the difference between measurement states recorded in the two files. The spatial resolution and range of the results for strain/temperature data can be controlled by adjusting the following data processing parameters:

- sensing range/integration width - the total DOFS length being analysed, [m];
- gauge length (GL) - the length of each virtual strain gauge, [m];
- sensor spacing (SS) - the spacing between each virtual strain gauge, [m].

When SS $= \frac{1}{2}$GL, the resulting strain or temperature measurement is considered to be quasi-continuous because the strain gauges cover the entire sensing range with no discontinuities. These parameters also allow the user to control the number of data points generated for a given sensing range: the number of data points (or the number of virtual strain gauges) is the sensing range divided by the sensor spacing. An exception is when certain primary measurements are included in the text file such as amplitude or spectral shift quality. In that case, the data processing parameters are overridden and the text file contains the maximum number of data points, at a resolution of 26109 points/m.

2.1.5 Python UI Automation

As mentioned in the previous sections, UI automation was used to take measurements and post-process the raw data into strain measurements. The scripts were adapted from [19] to each data collection procedure. The overall measurement procedure consisted of the set of steps shown in Figure 2.3. The script was calibrated by recording the location of the scan button manually. Then, measurements were taken and saved automatically using Python 2.7 with extended functionality from the `PyUserInput`, `schedule`, `audiere` and `time` packages.

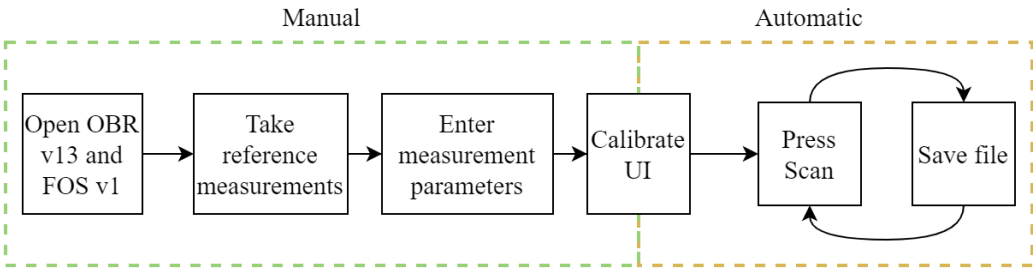

Figure 2.3: Procedure for taking OBR measurements

2.1.6 Measurement Noise

High levels of noise can render the OBR measurements unusable, as it is no longer possible to the actual measurement from the noise. However, even the measurements that are considered acceptable are not completely noise-free, as even the minutest deformations (e.g. due to the movement of air around a fibre) can be detected by the DOFS. Empirically, the threshold strain for an acceptable measurement is approximately ± 5 $\mu\epsilon$ [20]. The OBR manual [21] lists possible causes of excessive noise in measurements as follows:

- mechanical or acoustic vibrations;
- poor connections to the interrogation device (dirty, loose or broken connectors);
- excessively high curvature of the fibre;
- fibre is too long;
- interrogation device is uncalibrated;
- step size in the measurement is too small;
- large change in spectral shift within selected gauge length.

Studies employing DOFS sometimes discuss noise in the measurements as a side-topic, however, it is rarely the main focus. Fibres embedded in engineering structures can also suffer from microbending which causes increased levels of noise [20]. For example, embedding DOFSs between two layers of fibres in a composite laminate with different orientations causes bending on a very small scale. Reference [20] also mentions that fibres exposed to high pressures also resulted in noisy measurements, presumably due to damage in the fibre core. Unlike external mechanical vibrations, most of the other causes of noise are easy to address by using good working procedures.

2.2 Experimental Procedures

2.2.1 Preparation of the Optical Fibres

To be able to use the DOFS for any sensing application, the fibre must be prepared. A fully prepared optical fibre sensor is shown in Figure 2.4. Preparation of the OFs consists of splicing the OF with an FC/APC connector used for connecting the DOFS to the interrogation device. First, the polymer coating of the OF is removed with a butane torch, to expose the cladding. The portion of the fibre with the ferrule connector/angle physical contact (FC/APC) has a rubber jacket, which is stripped to reveal the cladding. The naked fibre ends must then be cleaned to avoid contamination and placed into a high-precision fibre cleaver to get a straight, perpendicular cut on the end of the fibre. Getting a straight cut is important as it ensures that the tip of the fibre is an optically-smooth surface [22], called a mirror zone, which minimises the signal attenuation at the splicing location. Finally, the two mating ends are spliced in a fusion splicer and the fused area is covered with a protective shrink tube. The attenuation at the fusion location, in the splice joint between bare and secondary coated OF, was checked to see if it was under the acceptable value of 0.1 dB. The average loss of the splice joints in the fibres used in the experiments was 0.05 dB.

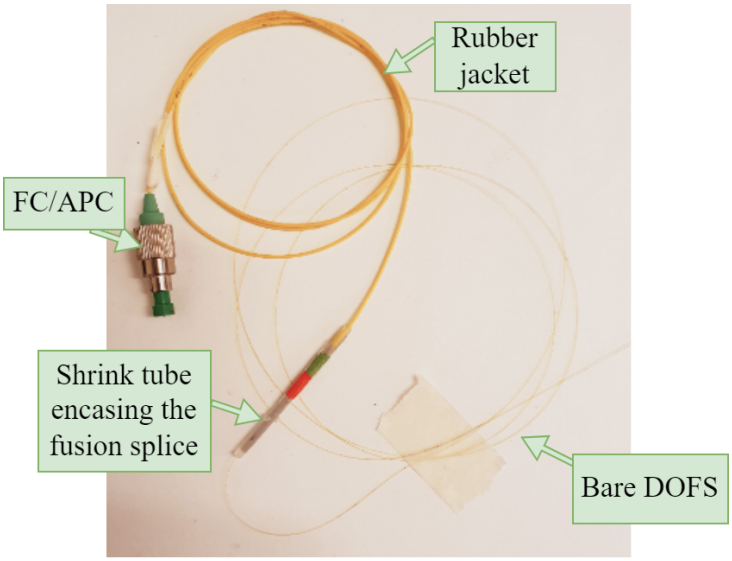

Figure 2.4: Bare DOFS attached to an FC/APC

2.2.2 Free-Hanging Fibres Setup

The first experimental setup was used to collect data for the tip-termination analysis and classification of disturbances in free-hanging fibres. A diagram of the experimental setup is shown in Figure 2.5 with approximate dimensions of individual components. The first portion of the bare DOFSs was contained in an airtight cardboard tube fixed by polystyrene discs at both ends. The fibres were secured to the discs with a hot-glue gun. The upper cardboard tube was used to shield the free-hanging fibres from external disturbances such as random flows of air and ambient acoustic noise. The second portion of the fibres was suspended freely in a steel mesh tube which only contained the excessive movements of the fibres. Two 12 V computer fans [23, 24] were placed opposite and facing each other at the same height and distance away from the mesh tube. The computer fans were powered by a variable power supply unit (PSU) and controlled by means of fast pulse width modulation (PWM) using an Arduino Uno microcontroller. The fans were intended to incite large-amplitude but low-frequency mechanical disturbances. The other disturbance source was a loud industrial vacuum cleaner, placed on the floor ca. 1 m away from the fibres and the tube setup as shown in Figure 2.6. The vacuum produced a constant acoustic sound, which caused low-amplitude but high-frequency movements of the fibre ends.

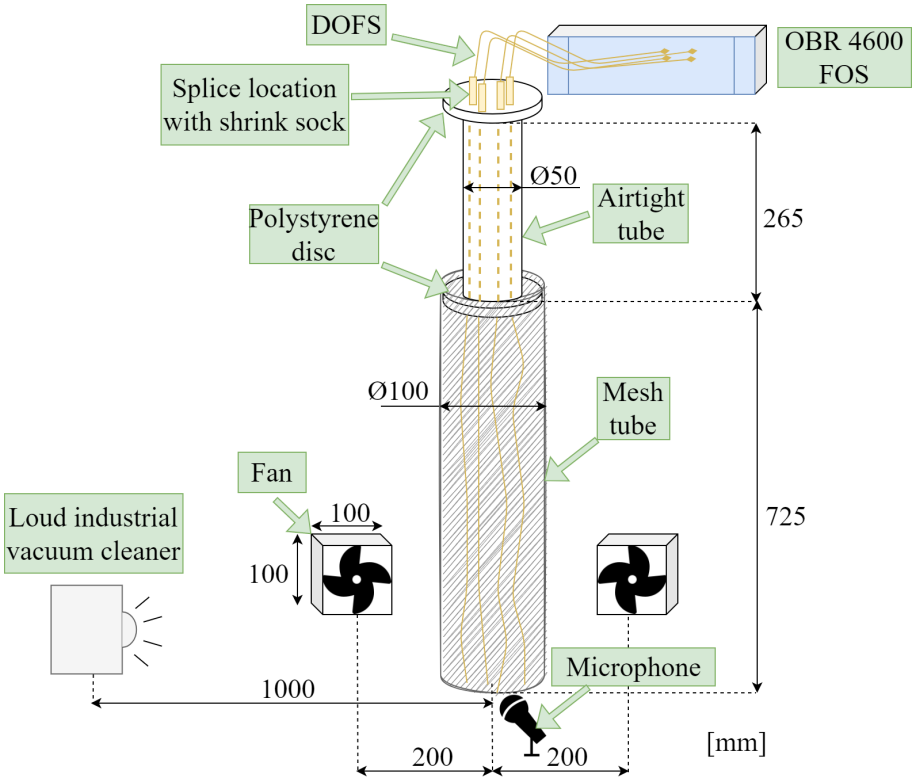

Figure 2.5: Experimental setup with free-hanging optical fibres (schematic)

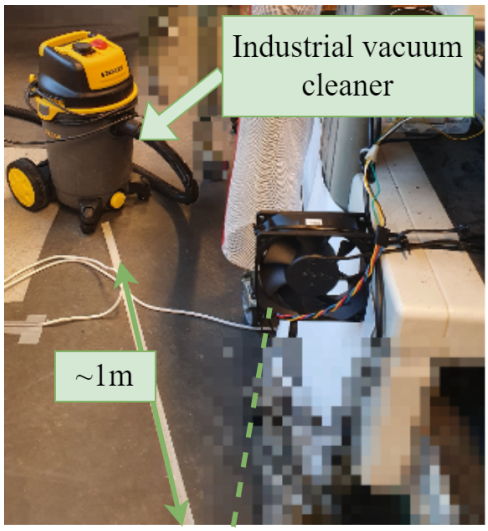

Figure 2.6: Placement of loud industrial vacuum cleaner

Figure 2.7: Examining the behaviour of the fibre ends

Two additional sources of data were a microphone (44 kHz sampling frequency) and a camera. The microphone was placed next to the steel mesh at the same height as the air fans to record the acoustic effect from the activated disturbances. The movement of the fibre ends was also recorded with a camera at the lower opening of the steel mesh as shown in Figure 2.7.

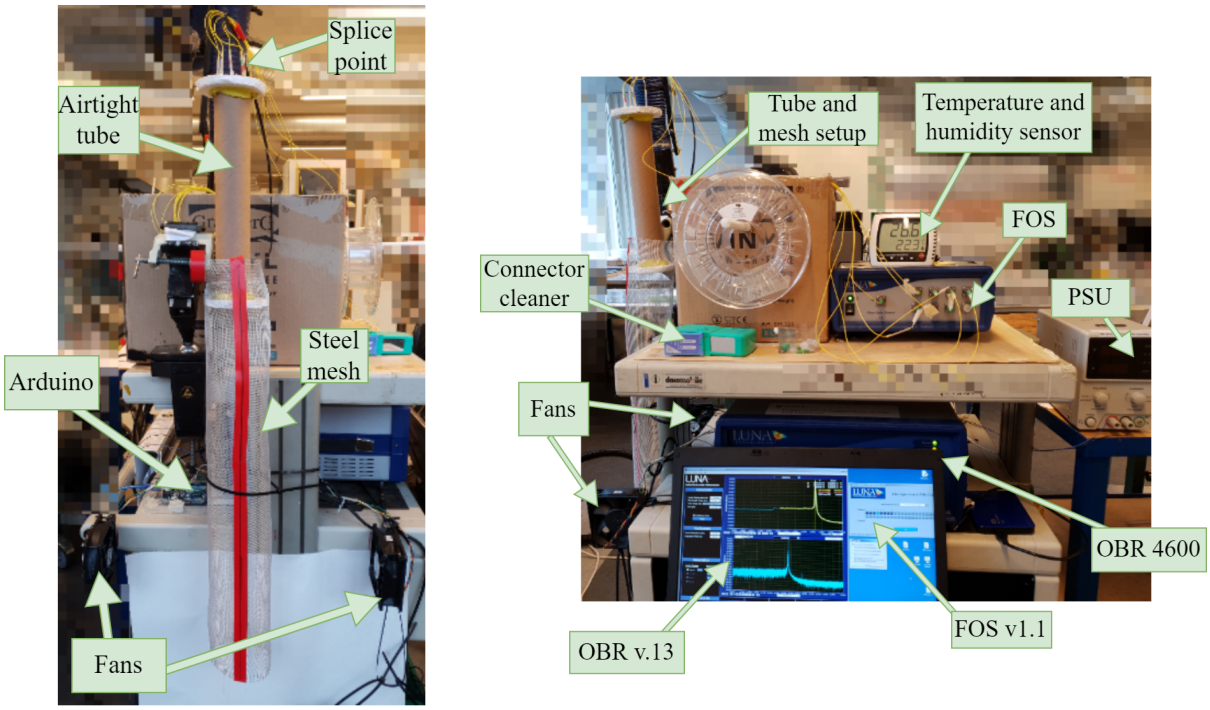

(a) Side-view

(b) Front-view

Figure 2.8: Experimental setup with free-hanging optical fibres (photos).

Figure 2.8 shows the whole physical test setup including the DOFS measurement system. The sensor fibres were connected to the fibre optic switch (FOS) which had eight channels, meaning eight fibres could be interrogated at any one time. The FOS was in turn connected to the *OBR 4600* interrogation device which sent the light pulse and measured the backscattered signal from the OFs. A PC was connected to the FOS to gather the data using the OBR software.

OFs are very sensitive to certain environmental factors such as temperature, strain and mechanical vibrations. A thermometer placed at the site of the experiment showed that the temperature in the lab changed by ca. ± 2 °C throughout the day. A temperature change of ± 1 °C produces strains of approx. ± 10 $\mu\epsilon$ [25], which would be interpreted as a baseline drift in the result. Hence, measurements for a given optical fibre were taken immediately after the reference measurement. The fibres were not detached from the FOS for the whole duration of the experiment.

2.2.2.1 Tip-Termination Experiments

As shown in Figure 2.2, there is a sharp increase in the optical signal attenuation at the end of the fibre due to the end-reflection. In the *OBR 4600* manual, it is noted that the end-reflection peak can sometimes make it difficult to take measurements near the end of the fibre [21, p. 184]. The first experiment aimed to determine the physical length of the fibre end that is affected by the the end-reflection. The experiment involved the following procedure, identical for six fibres (F1-F6): twenty measurements were taken using a Python script while the fibres were hanging freely as shown in Figure 2.5 with no deliberate disturbances. The raw amplitude curves were then analysed.

2.2.2.2 Disturbance States for Free-Hanging Fibres

In addition to the tip-termination analysis, a second set of experiments was carried out by using exactly the same experimental setup as described in previous sections (six free-hanging DOFSs suspended through two cylinders). This second experiment was designed for classification purposes, to use ML for identification of vibrational perturbations of very diverse origins. The sources of vibrations are hereby called measurement states or disturbance states.

Twenty measurements were taken for each of the disturbance states in the order listed in Table 2.2. In addition to this, twenty seconds of audio were recorded for each measurement state with the microphone placed between the fan and the mesh tube, as well as a ten-second video clip. In addition to the pure states *Norm, Vac* and *Fan1-4*, the measurement states were also assembled into a *Low* and a *High* group of composite states. The utility of *Low* and *High* composite states is explained in a later section.

Table 2.2: Descriptions of disturbance states

Measurement State	Description
Norm	Quiet room with minimal airflow. No deliberate[1] disturbances activated.
Vac	Loud industrial vacuum cleaner placed 1 m away from optical fibres and turned on. Pure acoustic effect, no movement of air observed around the fibres.
Fan1	Two opposite-facing air fans turned on at 1/4 maximum speed. Little visible movement in fibre ends.
Fan2	Two opposite-facing air fans turned on at 1/2 maximum speed. Moderate visible movement in fibre ends.
Fan3	Two opposite-facing air fans turned on at 3/4 maximum speed. Moderate visible movement in fibre ends.
Fan4	Two opposite-facing air fans turned on at maximum speed. Vigorous visible movement in fibre ends.
Low	A composite state consisting of {*Vac, Fan1*}.
High	A composite state consisting of {*Fan2, Fan3, Fan4*}.

[1] Some acoustic signals were present such as from air-conditioning fans and from cooling fans inside computers.

2.2.3 Bonded DOFS Setup

In the next set of experiments, data was gathered using DOFSs fixed to a long composite beam exposed to constant acoustic tones in the vicinity of its lowest eigenfrequency. This experiment investigated the response of the DOFS measurement to a controlled set of vibrations. The acoustic excitation frequencies were chosen close to the fundamental eigenfrequency of the beam. This way most of the acoustic energy is expected to convert to the mechanical energy of the beam which hosts the DOFS.

The physical setup for collecting OBR data consisted of a beam suspended by thin sewing thread over a speaker at $0.1L$ from the ends as illustrated in Figure 2.9. A DOFS was glued to the top of the beam in the centre with ethyl 2-cyanoacrylate glue, leaving approx. 300 mm of free fibre to account for the tip-termination noise from the fibre end. The other end was connected to the OBR interrogation device.

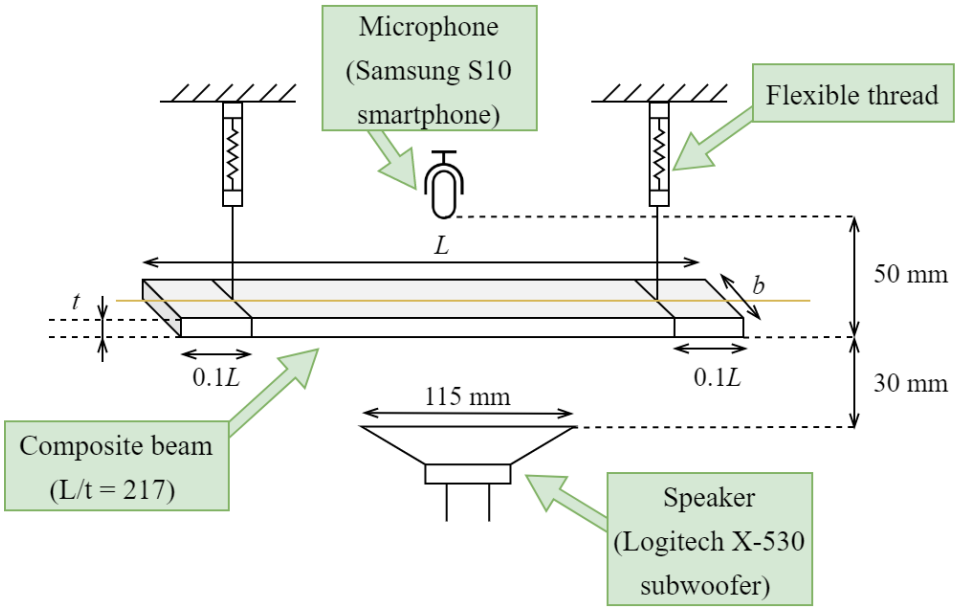

Figure 2.9: Experimental setup for DOFS attached to a long beam

The testing principle required the fundamental eigenfrequency of the beam. A three-point bending test was performed on the beam specimen to calculate the flexural Young's modulus using Equation 1. The slope, $\frac{dF}{dw}$, was estimated by linear regression on the elastic part of the load-displacement curve obtained from the bending test. The equation parameters are explained in Table 2.3.

$$E = \frac{dF}{dw}\frac{L_s^3}{4bt^3} \tag{1}$$

The fundamental eigenfrequency was calculated from Equation 2 from the ASTM E1875 standard [26], which is suitable for long beams with free-free boundary conditions.

$$f_1^2 = \frac{Ebt^3}{0.9465 T_1 m L^3} \qquad \text{where} \qquad T_1 = 1.000 + 6.585\left(\frac{t}{L}\right)^2 \tag{2}$$

Table 2.3: Properties of the composite beam

Symbol	Parameter	Value
b	Width of beam	19.8 mm
$\frac{dF}{dw}$	Load/displacement gradient	1.8 N/mm
E	Young's modulus	14.6 GPa
f_1	Fundamental eigenfrequency	48.0 Hz
L	Length of beam	250.0 mm
L_s	Span in test three-point bending test machine	100.0 mm
m	Mass of beam	8.7 g
t	Thickness of beam	1.15 mm

The geometries of the first three bending modes are illustrated in Figure 2.10, where the distance from the end to each node is marked.

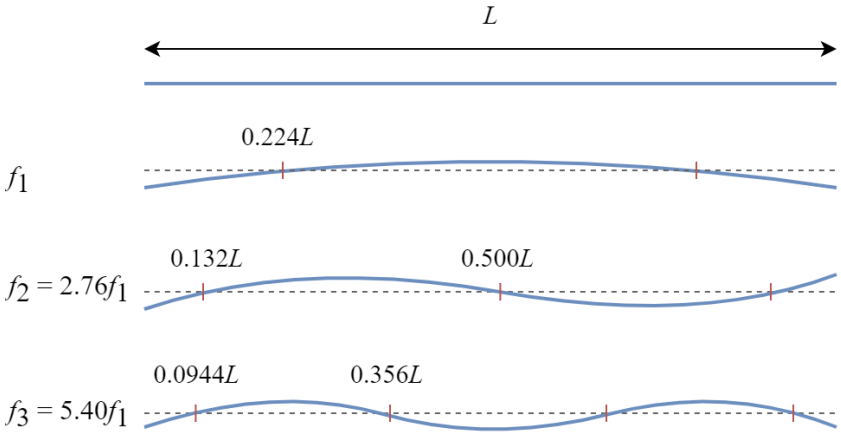

Figure 2.10: First bending modes of a free-free beam (adapted from [26]).

To gather data, the speaker was programmed to play a constant frequency and volume tone (of a sinusoidal waveform) continuously while measurements were taken using the *OBR 4600* interrogation device. Measurements were taken at twenty-one discrete frequencies in the range $[f_1 - 10,\ f_1 + 10]$ Hz, where f_1 is the fundamental flexural frequency of the long beam. Fifty strain measurements were taken for each discrete frequency at three different speaker volume levels. A microphone was positioned over the speaker and the beam to record the tone played by the speaker. Due to the large quantity of data collected, which took several hours per amplitude level, new reference measurements were taken on each day the measurement script was set to run.

2.3 Numerical Methods

Machine learning procedures encompass many numerical tools and data processing methods. The main steps in building a machine learning model are presented here along with the specific tools used in the development, followed by explanations and motivations behind the chosen model structures.

2.3.1 Code Structure

The most important libraries and their use in the project are described in Table 2.4. The libraries were used with Python 3.9 for ANN development and data visualisation.

Table 2.4: Python libraries and their uses

Library	Uses
`keras`	Provides high-level abstraction of ML and ANN models making it possible to build bespoke models with concise code.
`keras-tcn` [27]	Implementation of TCN.
`matplotlib`	Plotting tool.
`numpy`	Offers a wide range of mathematical operations for preprocessing data.
`pandas`	Allows for data from text files to be stored in DataFrame objects for analysis and processing. DataFrame objects are analogous to spreadsheets, which have basic mathematical functionalities.
`pyts` [28]	Helper functions for time series classification tasks.
`seaborn`	Tool to customise plots made using `matplotlib` and make statistical plots from `pandas` DataFrames.
`scipy`	Provides useful data pre-processing functions as well as functions for evaluating results.
`tensorflow`	The back-end mechanism for `keras`, making it possible to tailor models with low-level programming.
`tsaug` [29]	Time series augmentation functions.

Figure 2.11 shows how an object-oriented approach was employed to create the ANN model and data class. A data class makes it intuitive and easy to keep an overview of the pre-processing steps and the Keras interface makes it possible to customise models with extra functions and bespoke structures as well as reuse code between models. A `BaseANN` class was created using inheritance to use built-in model functions such as `train()` and `predict()` and for creating specialised supporting functions. The model structures were defined in separate TCN/LSTM classes, which inherited from the `BaseANN`.

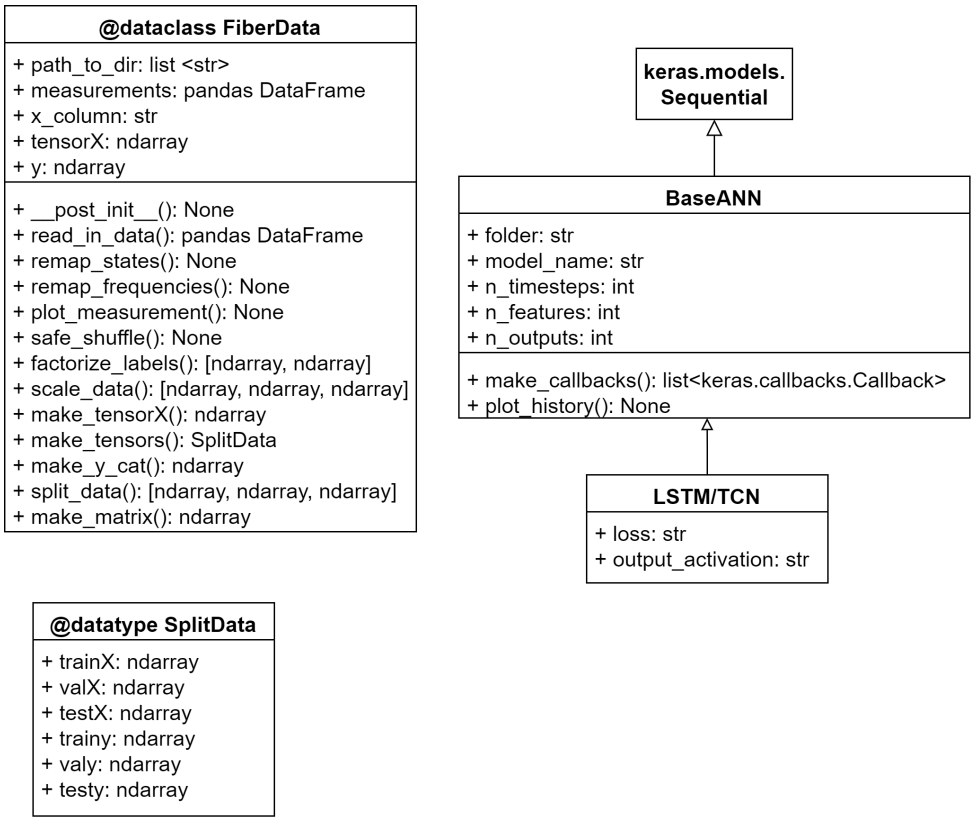

Figure 2.11: Diagram of the data class and `BaseANN` contents

2.3.2 Preparing Data for the Model

The strain data, which comes in a structured text file after OBR post-processing, must be extracted and prepared in such a way that makes it possible to feed it into the numerical model. Figure 2.12 shows how the complete DataFrame is divided into features and labels and training, validation, and test data. When the data is read in from the text file, each file is assigned a unique time series ID. The state, reference number, measurement number and fibre number are extracted by parsing the name of the file, which follows a predetermined naming convention. These values are stored in their respective columns in the DataFrame to be able to filter data quickly. The input must be compatible with the ANN, which means that the DataFrame must be rearranged into tensors containing training, validation and test data. Data exploration, scaling and augmentation are described in more detail in the following sections.

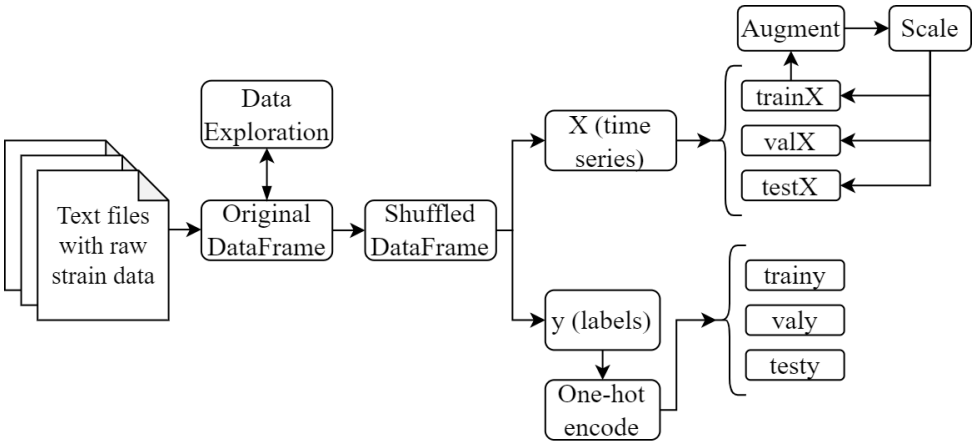

Figure 2.12: Overview of data the pipeline

2.3.3 Data Exploration

To get acquainted with the data on a statistical level and to be able to choose and preprocess features in a logical way it is important to understand any underlying trends in the data. At this stage, it can be helpful to plot the data, calculate statistics and see if there are any obvious differences between the classes which the model can exploit when making predictions. This process also reveals statistical differences in the data which can make it easier to interpret the performance of the model. In addition to well-known statistical concepts, a Gramian angular field (GAF) was employed for statistical visualisation of time series data. This concept is fairly new and is introduced in detail in Section 2.3.14. Furthermore, a quick introduction to fast Fourier Transform (FFT) is given in Section 2.3.15.

2.3.4 Data Augmentation

As a general rule, in machine learning, the more training examples that are fed into the model, the better the model performance. However, it is often not feasible or possible to gather very large amounts of data to due resource and time constraints. A powerful tool to address the lack of data is data augmentation, which is the process of injecting additional, modified records into the data set so that the model is exposed to a more comprehensive selection of examples. Data augmentation for sequential data is fairly new, so the quantitative effects are not fully known. However, some useful time series augmentation methods for classification problems have been highlighted in a recent publication [30]. Furthermore, the study concluded that combining several augmentation methods often gave better results than using just one. Some of the most useful data augmentation methods for time series classification problems are listed below.

- Flipping - multiplying the time series by -1.
- Cropping - extracting parts of the whole time series.
- Scaling - multiplying the whole or parts of the time series by a factor.
- Window warping - downsampling then upsampling again.
- Random time warping - expanding and contracting random parts of the series.
- Injecting outliers such as steps, slopes or spikes.

Before deciding on which augmentation methods to use or how to combine them with others, it is important to verify that the augmented data supports the distinctive characteristics in the raw data and will not confuse the model. One way to do this is to visualise the augmented data. For example, from Figure 2.13 it can be deduced that convolution is not a suitable augmentation method because it makes the curve look abnormal. The same can be said about time warping. Another verification method is training the network with the addition of augmented data and observing the effect on the final performance. Data augmentation can only be performed on the training data set.

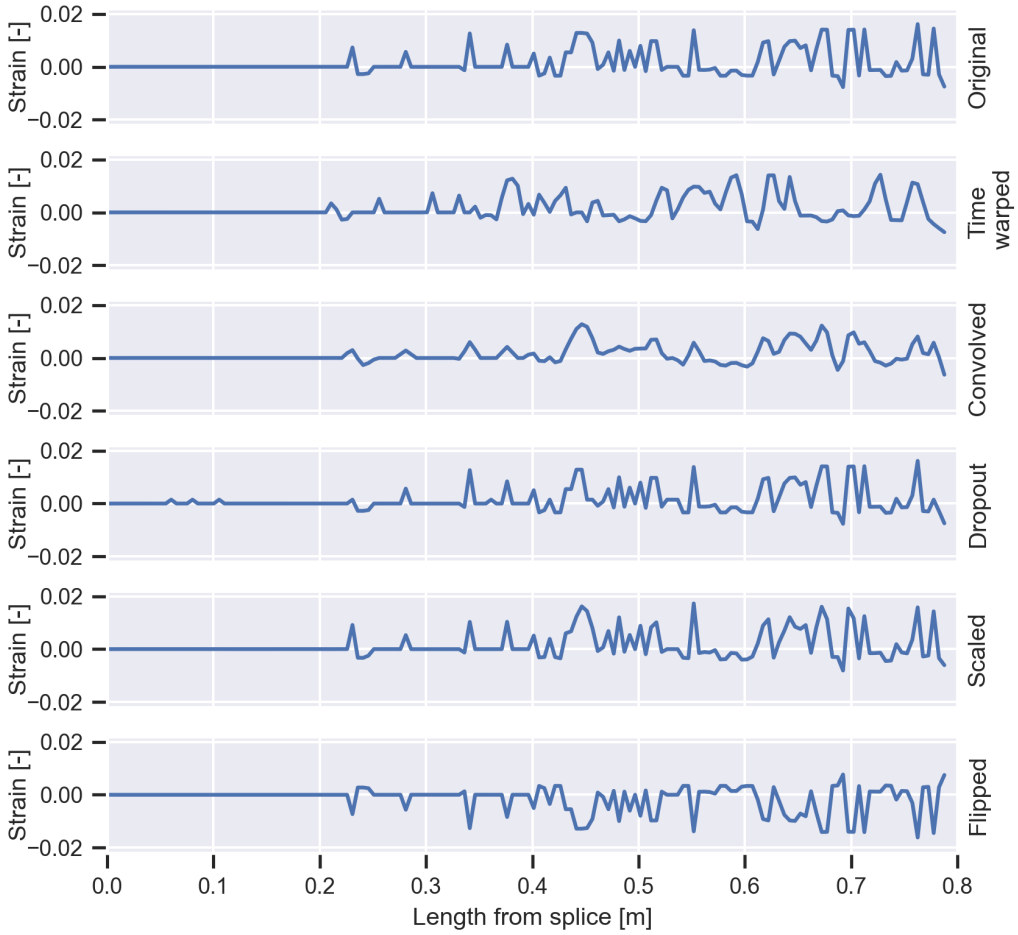

Figure 2.13: Augmentation of a series of strain values

2.3.5 Scaling

A basic feature engineering process is scaling the features to fit a specific range. This is especially important for ANNs because it reduces the risk of gradients exploding due to very high values. The scaling algorithm must be chosen appropriately for the data set. For a data set with many outliers, the recommended scaler is *RobustScaler* [31] as it scales values based on the interquartile range, rather than the minimum and maximum values of the feature. To prevent data leakage, a scaler is fit only on the training set and the same scaler is used to transform the validation and test sets. In this context, data leakage is when information from the test and/or validation set is included in the training set when the

model is created. Fitting a scaler on the whole data set would mean that information about values from the validation/test data sets would have "leaked" into the training set. Only fitting the scaler on the training ensures that the validation and test sets are truly unseen.

2.3.6 Labels

The labels also have to be preprocessed appropriately. For networks that make categorical predictions (e.g. classification tasks), the number of output neurons is equal to the number of categories or classes. Labels are encoded into vectors using one-hot encoding as described in [9]. For continuous predictions, where there is only one output neuron per feature, the labels are simply normalised (scaled between [0, 1]).

2.3.7 Training

Training the network essentially consists of feeding data into the network, allowing the network to make a prediction, checking the prediction against the true label and adjusting the network parameters accordingly. The aim of training is to minimise the loss function, which is a function used to express the penalty between the model prediction and the label.

One of the most important parameters in training is the learning rate, which defines the constant with which the gradient adjustment is multiplied before it is added to the network parameters. A high learning rate allows for larger updates but can cause the loss to overshoot the minimum. With a low learning rate, the parameters are updated in smaller increments, but this can cause training to be unnecessarily slow. A common approach is to have a high learning rate at the beginning of training to make big gradient adjustments followed by a gradually decaying learning rate to make smaller adjustments and locate the loss minimum more accurately.

Another important aspect is the number of training epochs. An epoch is completed when the network has processed all the training data to perform adjustments to all of the weights. An epoch can take several seconds to several minutes to complete, therefore it is important to continuously save the network parameters during training to save future computation time. The training time must be balanced: too few epochs can give a sub-par performance, whilst training the network for too long can cause the network to overfit. A common sign of overfitting is that the validation loss starts to increase, whilst the training loss continues to decrease because the network starts to memorise the specific training data rather than generalising. Similarly, a comparison between training, validation and test accuracy also gives an indication of how well the network has generalised. Callback functions used during training, some of which help to mitigate the issue of over-fitting, are listed in Table 2.5.

Table 2.5: Callback functions used during training

Function	Use
`CSVLogger`	Saves the training and validation loss to be able to plot them later.
`EarlyStopping`	Stops training when validation loss ceases to decrease to reduce overtraining.
`LearningRateScheduler`	Reduces the learning rate value after a certain number of epochs to make large updates to the weights at the start of training and finer updates later on.
`ModelCheckpoint`	Saves model weights after every epoch.

2.3.8 Regularisation

Regularisation can be used to improve the generalisation of the model. Whilst all ML models seek to minimise the loss function, adding regularisation also seeks to minimise the complexity of the model in addition to the loss. Minimising the complexity in a balanced way makes the network more generalised, which means it can recognise complex patterns more reliably in data that it has not seen before. Some regularisation techniques are dropout, normalisation and L1/L2 regularisation.

Dropout removes a set fraction of connections between neurons in the ANN. This leads to fewer connections between neurons and thereby a less complex model.

Normalisation during training such as batch or layer normalisation makes the weights more stable because the spread of weight values is restored between each layer. Preserving the distribution of values makes it possible to train the network for longer as it reduces the effect of covariant shift [32], where networks become very good at classifying from inputs which share the same mean and variance but struggle to generalise to inputs not sharing the same characteristics.

L1 and L2 regularisation, also known as Lasso and Ridge regression help with generalisation as well. Both methods work by adding the sum of the weights multiplied by a small coefficient to the loss function, making a small adjustment to the weight. Less important weights are gradually reduced to zero or near zero, making the network more sparse.

2.3.9 Evaluation

Discrete categorical predictions, where the prediction classes are treated individually, can be visualised in a confusion matrix. An arbitrary confusion matrix is shown in Figure 2.14. The confusion matrix makes it possible to visually analyse ANN predictions. For example, it makes it possible to see which classes of data the model often confuses. The average accuracy can be computed to quantify the performance of a model, as demonstrated in Equation 3, where M is the confusion matrix and n is the number of classes. One important assumption for this metric to be valid is that the classes in the data set are balanced, that is to say, each class has more or less the same number of true labels. For imbalanced data sets, the weighted average would be more appropriate, as it would take into account over- and under-represented classes. In

this study, the classes are represented fairly evenly, so the average accuracy from Equation 3 is used as the main metric.

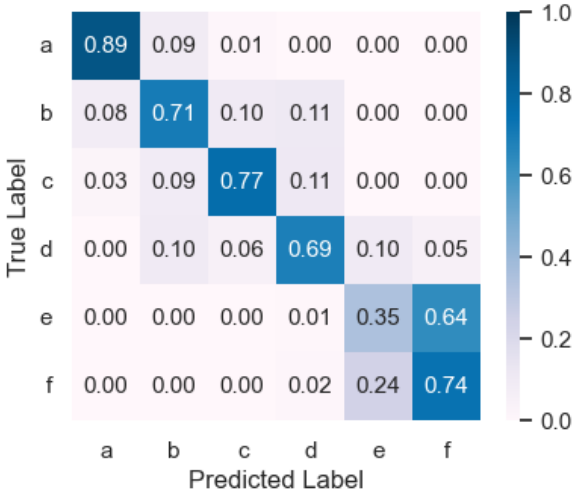

Figure 2.14: Confusion matrix for a set of arbitrary predictions (classes a, b, c, d, e, f)

$$\begin{aligned} \text{Accuracy} &= \frac{\text{tr}(M)}{n} \\ &= \frac{4.15}{6} \\ &= 69\% \end{aligned} \tag{3}$$

In cases where the class values are related and belong on a continuous scale, a different loss function and evaluation method can be more informative, namely mean absolute error (MAE). Figure 2.15 shows two extreme examples of arbitrary predictions. The diameter of the circle corresponds to the number of predictions for a specific class; the larger the marker, the more points there are at the same location. Consequently, the more accurate the predictions, the larger the circles on the diagonal line. The colour corresponds to the MAE, for which an empirical cumulative distribution function (ECDF) plot is shown to the right of the prediction grid. When predictions are more accurate, the ECDF increases more slowly.

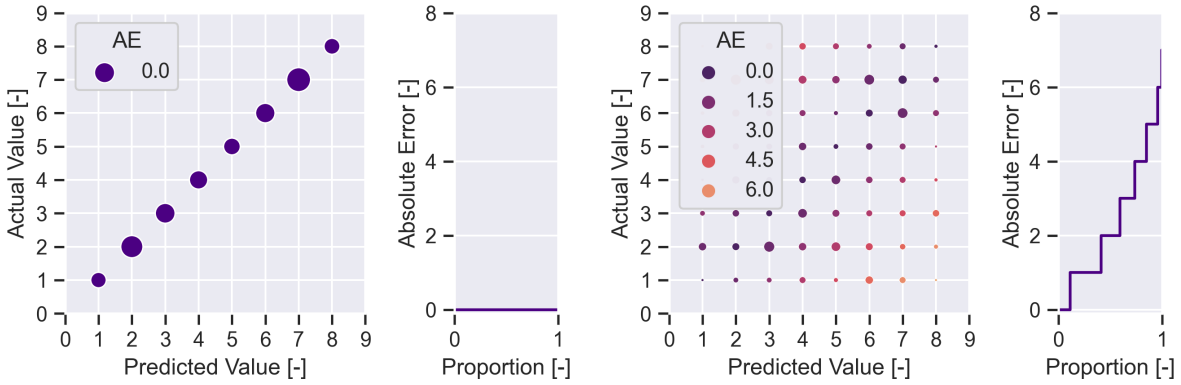

(a) Correct predictions

(b) Random predictions

Figure 2.15: Visual evaluation methods for predictions of continuous classes 1-8

2.3.10 Long Short-Term Memory

Recurrent neural networks (RNNs) are a type of ANN which are typically used for sequential data, such as time series data because outputs from previous inputs are used as inputs for proceeding layers. RNNs process data in sequences to preserve the time order. An LSTM is a special type of RNN network which addresses a major limitation of regular RNNs - the vanishing/exploding gradients problem. An LSTM block is illustrated in Figure 2.16. By combining weighted outputs from the preceding cell **h**(t-1) as well as outputs from several time steps back in time **C**(t-1) with inputs from the current time step **x**(t), an LSTM network can remember longer sequences than a conventional RNN, which only combines **h** (t-1) and **x**(t) [9]. LSTM ANNs were discussed in more detail in the preceding Project thesis [9].

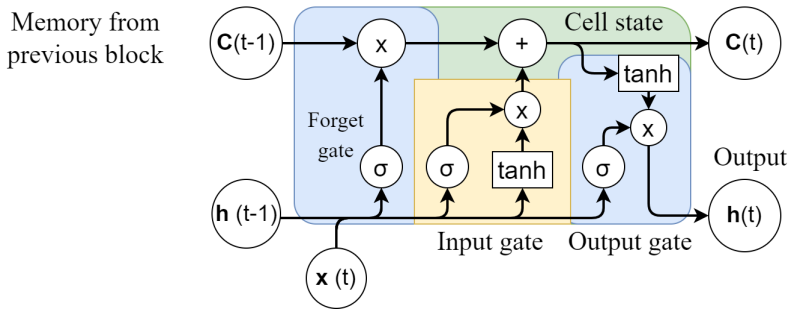

Figure 2.16: Diagram of an LSTM (from [9].)

2.3.11 Temporal Convolutional Networks

Temporal convolutional networks (TCNs) are a new type of network structure, which first emerged in 2017 [33]. TCNs can be used to model sequential data while exploiting the parallel processing capability that convolutional networks provide [34]. The main advantages of TCNs are that they can train several times faster than RNNs and model long sequential patterns [33]. Contrary to LSTM networks, TCNs can take in inputs of different lengths, which potentially makes them a more versatile network structure.

A convolutional neural network (CNN) is a neural network which includes convolutional layers. In a 1-D convolutional layer, a kernel or filter is passed across the time series. The result is the dot product of a section of the data series and the filter as illustrated in Figure 2.17. Convolutional layers are used to detect features in data. TCNs use dilated casual convolution. They are "casual" because they only use data points from the past and "dilated" because a certain number of data points are skipped, making it possible to extract features from longer sequences more efficiently than LSTM networks [35]. The hierarchical structure depicted in Figure 2.18 with exponentially increasing dilation factors allows the TCN network to capture features of different lengths.

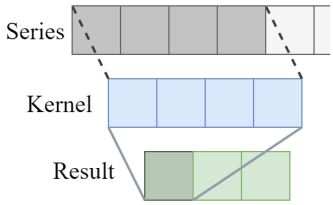

Figure 2.17: 1-D convolution

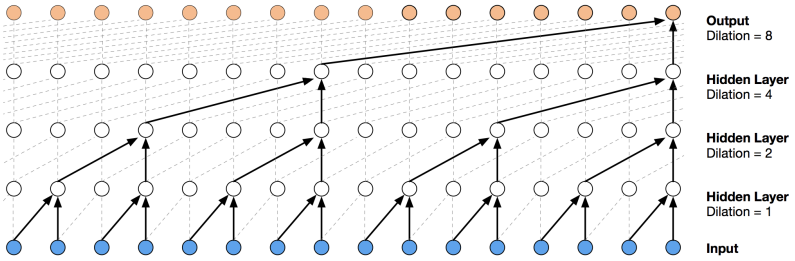

Figure 2.18: Structure of TCN layer with dilated convolution (from [35])

The number of steps the network observes in the past is called the receptive field, R. Equation 4 describes how the size of the kernel, K, the number of layers, L, and the dilation factors, d can be used to calculate R [27]. The receptive field should be adjusted appropriately for the sequence length. If it is not possible to choose parameters such that the receptive field length matches the sequence length, the receptive field will be padded with zeros. Some of the hyperparameters that can be used to build and tune the TCN network are given in Table 2.6.

$$R = 1 + 2^{L}(K-1) \cdot \sum_{i}^{n} d_i \tag{4}$$

Table 2.6: A description of selected TCN hyperparameters

Hyperparameter	Description
`dilations`	Dilated convolution spacing for each layer.
`dropout rate`	Fraction of connections that are zeroed out to make the network simpler and more generalised.
`kernel initializer`	Initialises the weights based on a chosen distribution.
`kernel size`	Size of kernel used in convolutional layers. A smaller kernel size means that the output will depend more on the most recent time steps.
`nb filters`	Number of filters in convolutional layer.

2.3.12 ANN Development Process

The development process employed to decide the final ANN model structure and parameters is shown in Figure 2.19. Parameters were tested by training the network and by observing the loss curves during training and evaluating the performance accuracy Equation 3. Visualising and evaluating the predictions made on training, validation and test sets are useful tools in deciding which parameters to adjust next. If predictions are poor for all data sets, it may mean that the network does not have enough neurons to model the data [36]. Alternatively, it could mean that there is no correlation between the input data and the labels. The solution may be to increase the network complexity by increasing the number of neurons in a layer or the number of layers in the network. Another possibility is that the training set predictions are very high, but the validation and test set performances are poor. This would suggest that the network is overfitting. Hence, it could be beneficial to increase regularisation rates, employ normalisation methods or add a dropout layer.

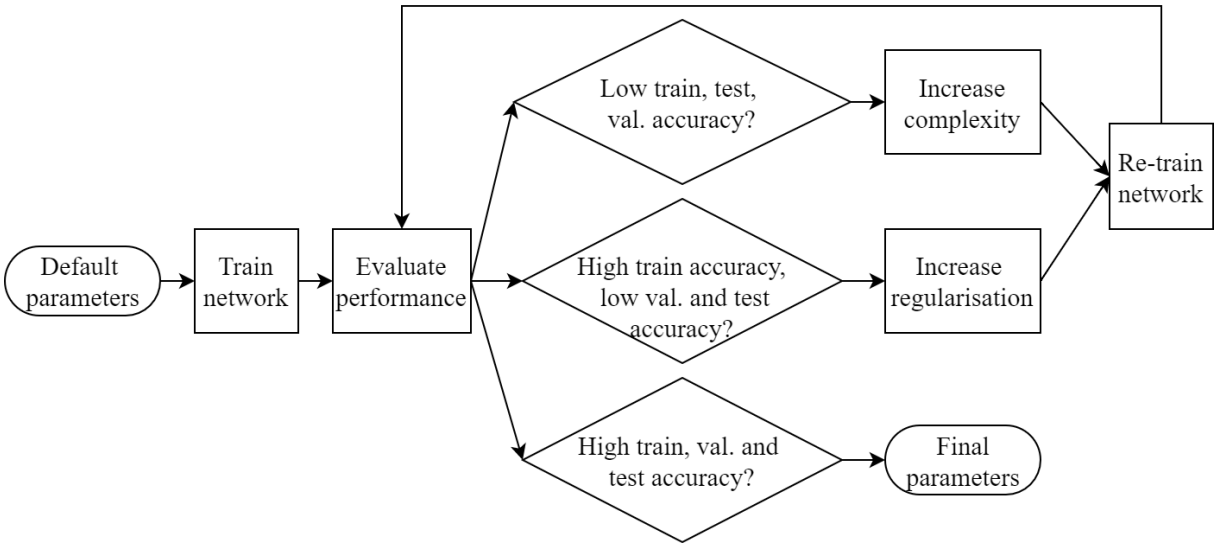

Figure 2.19: ANN development process

2.3.13 Final ANN Structures

For the first classification task, employing the free-hanging DOFS data, two LSTM ANNs and two TCNs were used. All of the categorical models used the categorical cross-entropy loss function. Time series lengths of 150 data points were generated from the original DataFrame, giving a total of 4795 time series. The training, validation and test split was 60%, 20% and 20% respectively for all models. Trial and error revealed that the most effective data augmentation method was flipping the time series vertically (i.e. multiplying by -1), whereas other methods caused a decrease in performance. Hence, only time series augmented by flipping were added to the training data. The network layer parameters for the LSTM ANNs are presented in Table 2.7. The LSTM networks were trained with a learning rate of 0.0001 and a batch size of 16.

Table 2.7: Two LSTM model structures for free-fibre disturbance classification

Layer	Layer Type	Number of Units	Layer Parameters
1	LSTM	32	-
2	LSTM	16	L2-regularisation of 0.01 for kernel, recurrent and bias weights
3	Dropout	16	Rate: 0.2
4	Fully Connected	6 (3)*	Softmax activation

*Two networks were developed. The only difference was 6 or 3 output classes.

The TCN structures are shown in Table 2.8. The TCN networks were trained with a batch size of 8 and a learning rate of 5e-5 to 8e-5 for ten epochs and exponentially decaying learning rate above ten epochs. The receptive field size for this network was 187. Similar to the LSTM models, the only difference in the models is the number of output classes (6 or 3).

Table 2.8: Two TCN model structures for free-fibre disturbance classification

Layer	Layer Type	Number of Units	Layer Parameters
1	TCN	64	kernel size: 4 kernel initialiser: Glorot uniform dropout rate: 0.10 dilations: [1, 2, 4, 8, 16] use_layer_norm : True/False
2	Fully Connected	6 (3)	Softmax activation

The second prediction task was to classify the frequency of acoustic vibrations for DOFS bonded to a vibrating beam structure. Two different TCN structures with one TCN block were used in different ways. The layer parameters for both TCNs are shown in Table 2.9. The first TCN was trained to predict frequencies categorically, using one-hot-encoded labels, similar to the preceding task. The second TCN had only one output neuron, which predicted a value between 0 and 1, representing a prediction in the

normalised continuous frequency range. This network did not require an output activation function and used mean squared error as the loss function. The receptive field for these networks was 311.

Table 2.9: TCN model structures for frequency predictions with a DOFS bonded to a vibrating beam.

Parameter	**Categorical TCN**	**Continuous TCN**
nb_filters	64	32
kernel_size	6	6
kernel_initializer	Glorot uniform	He normal
dropout_rate	0.30	0.20
dilations	[1, 2, 4, 8, 16]	[1, 2, 4, 8, 16]
use_layer_norm	True	True
use_skip_connections	True	False
Number of outputs	21	1
Output activation	Softmax	-

2.3.14 Gramian Angular Field

Originally proposed as an encoding method for processing time series with CNN models, Gramian angular fields (GAFs) are an intuitive way to visualise time series [37]. Therefore, GAFs can be useful in the data exploration stage in order to visualise time series classes. GAFs are a modified version of the Gram matrix or metric, G, where each element is the inner product of two vectors. To calculate the GAFs for a vector X containing a time series with n data points, the procedure is as follows: The vector elements are scaled down to a range of [-1, 1] and each point is encoded as a polar coordinate by taking the arccos of each value as shown in Equation 5.

$$\begin{aligned} \phi_i &= \arccos x_i \\ r_i &= \frac{t_i}{N} \end{aligned} \tag{5}$$

Then, the Gramian matrix is computed by Equation 6 where k is the temporal difference between two points in the time series. As a result, the diagonal, where $k = 0$ represents the original time series, and the matrix is always symmetrical.

$$\begin{aligned} G_{i,j \mid i-j=k} = < x_i, x_j > &= \cos \phi_{i,j} \\ &= \cos\left(\phi_i + \phi_j\right) \\ &= \cos(\arccos x_i + \arccos x_j) \\ &= \cos(\arccos x_i \cos \arccos x_j) - \sin(\arccos x_i \cdot \sin \arccos x_j) \\ &= x_i \cdot x_j - \sqrt{1 - x_i^2}\sqrt{1 - x_j^2} \end{aligned} \tag{6}$$

In matrix form, this allows for the Gramian angular summation field (GASF) and Gramian angular difference field (GADF) to be calculated as represented by Equation 7 and Equation 8 where X is the transformed time series and I is a unit row vector.

$$\text{GASF} = \cos(\phi_i + \phi_j) = X'X - \sqrt{I - X'^2}\sqrt{I - X^2} \tag{7}$$

$$\text{GADF} = \sin(\phi_i - \phi_j) = \sqrt{I - X'^2}X - X'\sqrt{I - X^2} \tag{8}$$

Some basic example plots of GADFs are shown in Figure 2.20. Noisy signals produce a chequered pattern, whilst noiseless and more regular signals have distinct areas or stripes of solid colour. An image size of 24 $\times$ 24 has been chosen for the GADF matrices for simplicity, meaning that the signal differences are discretised into 576 individual matrix cells. For data sequences with more than 24 points, the dimension is reduced to fit the image size using piecewise aggregate approximation (taking the mean of adjacent points) [28].

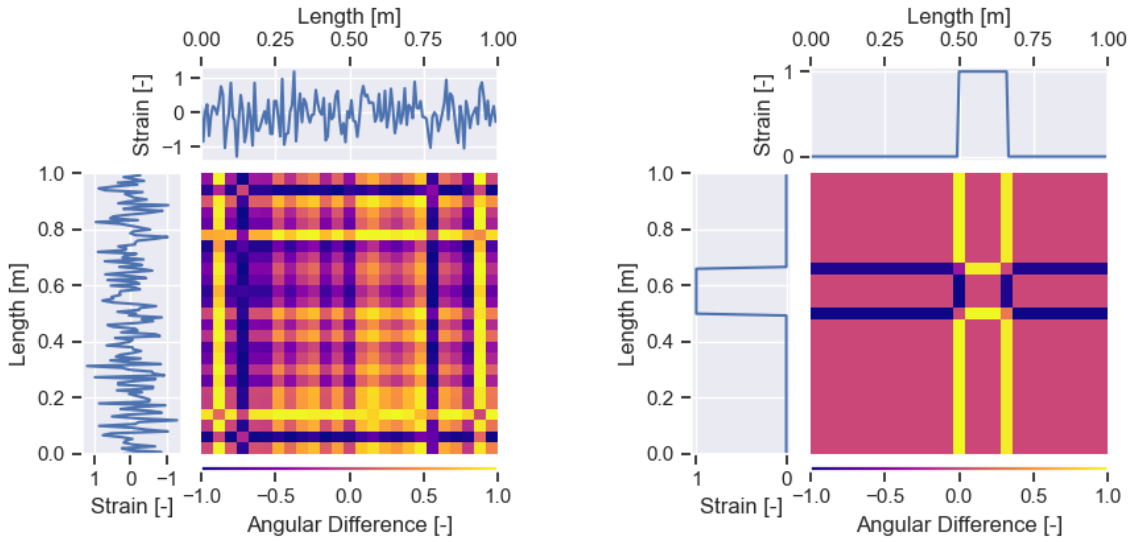

(a) Gaussian noise

(b) A square signal

Figure 2.20: GADF plots for two artificial strain measurements

2.3.15 Fast Fourier Transform

Frequency analyses can be used in several stages of the data analysis: investigating the output of the disturbances in Table 2.2, finding the eigenfrequency of a vibrating structure and verifying the speaker output in the acoustic disturbance setup (Figure 2.9). A simple way to accomplish a frequency analysis of a time series signal is by using a fast Fourier transform (FFT). The `scipy` package in Python provides functions to perform an FFT on a sound file in .wav-format. Figure 2.21 shows examples of FFTs of three artificially-generated noise signals.

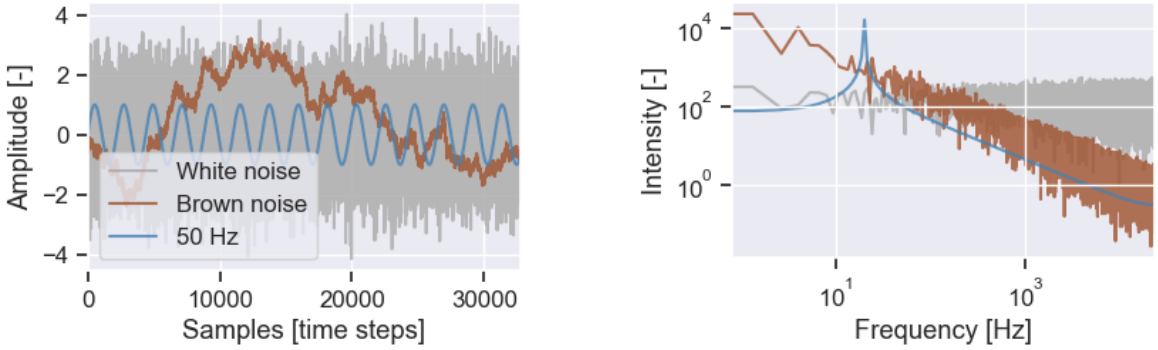

(a) Original signals

(b) Transformed signals

Figure 2.21: Fast Fourier transforms of artificial signals

3 Experimental Results

The data analysis procedures and the main experimental outcomes are presented in this section, starting with free-hanging DOFS experiments. The free-hanging experimental setup was used to investigate two problems: determining the tip-termination end reflection length for DOFSs and classifying the disturbance states on free DOFSs by using different ANN approaches. Following that, the results from a DOFS bonded to a composite beam structure are presented. The results of each experiment are discussed separately.

3.1 Tip-Termination Analysis

The aim of the tip-termination experiments was to determine how far back the end-reflection extends along the fibre. End-reflection is viewed as a light signal overload that can potentially corrupt the DOFS measurement, and should therefore be excluded from experimental data. This task was accomplished by analysing raw amplitude curves of free-hanging OFs.

3.1.1 Data Analysis

The amplitude curves for any kind of DOFS measurement fluctuate around a steady amplitude level. To smoothen the curve, a moving average (MA) was calculated for the raw amplitude data as shown in Figure 3.1a. The section between Q1-Q3, where Q1 and Q3 are one quarter and three-quarters of the total ca. 1 m sensing range respectively, was considered to be the baseline signal, unaffected by the end-reflection. The mean (μ) and standard deviation (σ) of the baseline MA curves were calculated for the section bound by Q1 and Q3. Since loss amplitude is the primary OBR data (see Section 2.1.4) the spatial resolution of data points is 26109 per 1 meter of DOFS length.

The cut-off length, i.e. the length of the DOFS affected by tip-termination is illustrated in Figure 3.1b. Equation 9 defines the cut-off criterion used where MA_{100} denotes a moving average with a window of 100 data points and $\mathrm{MA}_{100\cdot10}$ is the same moving average once more averaged over 10 points so that the cut-off line would not become located at a place where the amplitude happens to deviate from the MA by a large amount due to a random fluctuation. The robustness of the numerical procedure for cut-off length measurements was verified visually over many plots analogous to Figure 3.1b.

$$\mathrm{MA}_{100\cdot10} > \mu_{\mathrm{MA}_{100}} + 3\sigma_{\mathrm{MA}_{100}} \tag{9}$$

3.1.2 Results of Analysis

After analysing the amplitudes from all six fibres, the end-reflection length results were assembled in Table 3.1. The data from fibre F4 gave a negative length value and was considered to be anomalous. This result was labelled as an outlier in Table 3.1. The abnormal value may be because fibre F4 had a weak end-reflection peak (as shown in Figure 3.3) due to poor tip-termination quality. The overall mean and standard deviation end-reflection length calculated in Table 3.1 is therefore based on five OFs, where

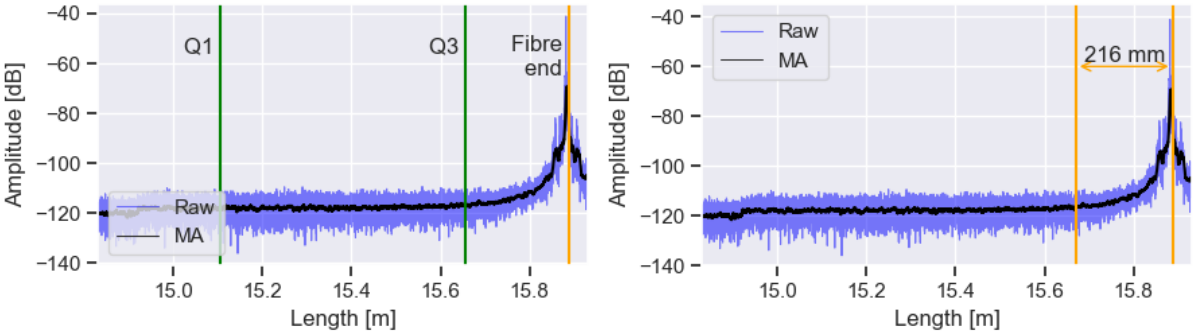

(a) Labelled graph sections used for calculations **(b)** End-reflection cut-off length based on the 3σ criterion

Figure 3.1: Example plot of amplitude (fibre F1, measurement 1) using a window size of 100 data points

μ_{length} is the mean end-reflection length for each OF. The coefficient of variation (CV) is calculated from CV $= \frac{\sigma}{\mu}$. In trial calculations, the MA curves were generated with window lengths of 100-1200 data points. Shorter window lengths reflected local changes better, whilst longer window lengths gave smoother MA curves but lagged visibly behind the raw amplitude curve. However, due to the high data point density (26109 points/m), the final result was approximately the same with all moving average windows, ranging from 121 mm to 161 mm. As a trade-off between capturing the local variations in data and having a sufficiently smooth curve, the window length used to calculate the final results was set to 100 data points. Limits using 2, 3 and 4 standard deviations for the criterion in Equation 9 were also tested. The number of acceptable standard deviations was eventually set to 3 because using fewer standard deviations as the limit often resulted in the cut-off point being visibly placed too far towards the baseline region of the OF.

Table 3.1: Results for each DOFS with the MA window length of 100 (statistics over 20 repeated measurements per fibre).

Fibre No.	μ_{length} [mm]	σ_{length} [mm]	CV [-]	Max. amplitude [dB]
1	221	19.2	0.087	−41.1
2	200	3.00	0.150	−37.7
3	109	3.11	0.287	−49.0
4	−0.397	1.68	−4.23	−69.7
5	63.2	16.4	0.259	−56.6
6	114	25.0	0.173	−47.1
All*	147	64.7	0.439	−46.3

*Excluding F4

Figure 3.2 shows a positive correlation between the mean end-reflection length for a given fibre (μ_{length}) and the maximum amplitude for the end-reflection signal attenuation: the higher the end-reflection amplitude, the longer the mean end-reflection length.

Example plots of individual cut-off lengths from two different DOFSs are presented in Figure 3.4. Signals from fibres F1 and F5 have been specifically selected to illustrate the differences in the end-

reflection peak shapes and cut-off lengths. The transition between the flat baseline part of the MA curve to the end-reflection peak is sharper in Figure 3.4b than in Figure 3.4a, which gives a shorter cut-off length on average.

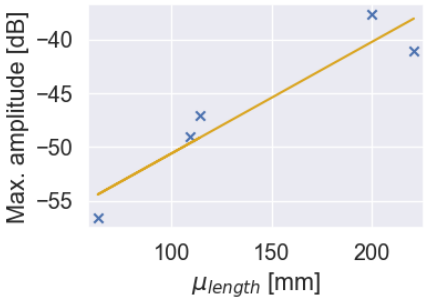

Figure 3.2: Positive correlation between μ_{length} and the maximum end-reflection amplitude

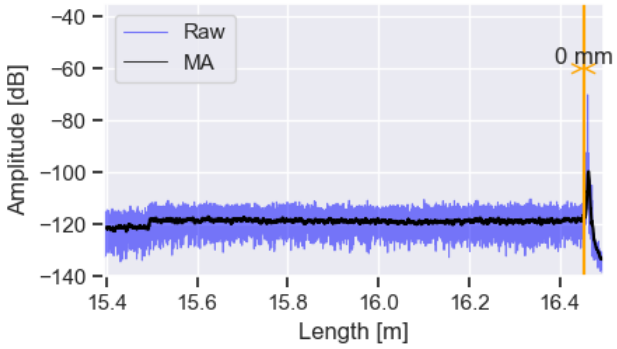

Figure 3.3: Amplitude curve from fibre F4

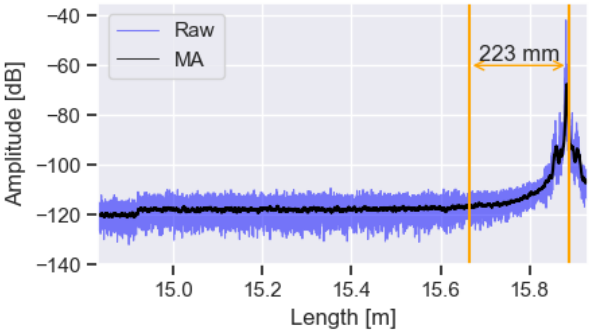

(a) Fibre F1, measurement 3

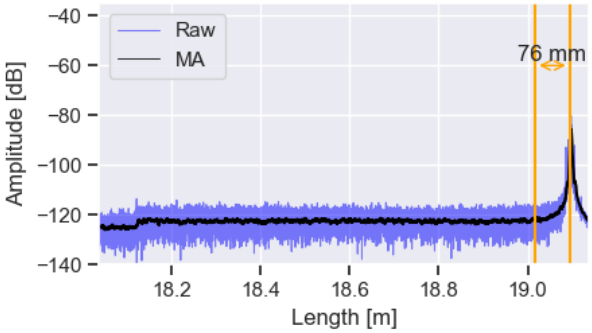

(b) Fibre F5, measurement 7

Figure 3.4: Results from two DOFSs with different end-reflection peaks

3.1.3 Discussion

The amplitude curves of individual DOFSs are unique, depending on how the actual fibre has been cut. In particular, the end-reflection peaks exhibit different shapes, where some have a sharper transition from the flat baseline to the peak than others. This is likely due to the shape of the fibre end. A straight perpendicular cut would presumably cause more light to be reflected back into the fibre core and lead to a lower end-reflection attenuation peak. Another source reports that strong reflectance peaks (particularly those >-45 dB) tend to have broader bases [21, p. 164]. The positive correlation observed in Figure 3.2 is in line with this observation. Furthermore, there is a large difference between the data points below and above -45 dB. The same trends can also be observed in both graphs in Figure 3.4.

The variations in different amplitude curves make it challenging to judge exactly where the end-reflection effect ends. In some fibres, such as fibre F1 in Figure 3.4a, it is difficult to tell where the MA amplitude starts to increase because the transition is gradual. Judging by eye, the cut-off length

could be placed anywhere between 15.6 m to 15.7 m (250 mm to 150 mm from the end). However, the $\mu + 3\sigma$ threshold is crossed first at 223 mm from the end. At the same time, a sharp increase in the MA amplitude occurs only after 15.8 m (during the last $\approx$ 20 mm). This raises the question: does the end-reflection effect begin where there is a sharp increase in amplitude or when there is already a slight increase in amplitude? In curves with sharper transitions, such as in Figure 3.4b, it is easier to see the start of the end-reflection. This observation is also in accordance with the CV differences in the overall result in Table 3.1. The coefficient of variation (CV) between μ_{length} values for different physical OFs is significantly higher than differences in repeat measurements for each individual fibre, suggesting that is difficult to establish an accurate universal cut-off length for all OFs.

The data from fibre F4 was considered to be anomalous because the peak amplitude was approximately 20 dB lower than for the rest of the fibres, which resulted in a less-pronounced MA amplitude (Figure 3.3) and subsequently, negative cut-off lengths. Again, the poor end-reflection peak quality can be attributed to irregularities in the fibre end.

The overall mean cut-off length was 147 mm with a standard deviation of 64.7 mm. However, due to curves with very gradual transitions towards the end-reflection peak, this result is likely an overestimation. With variations in the fibre-end cut quality to be expected, the cut-off point for future experiments should be chosen conservatively. Therefore, in the following experiments, the data from at least the last 150 mm from the DOFS end should not be used in the post-processing stage.

3.2 Classification of Vibrational Disturbances Using Free-Hanging DOFS Data

In this investigation, experimental strain data from the OFs is analysed using LSTM and TCN structures. This section builds directly on the work presented in [38], only adding the TCN architecture consideration which has not been tested on DOFS data before. The aim was to establish whether ANN models could classify the source of different vibrational disturbances on free-hanging DOFSs (presumably the simplest test case).

3.2.1 Data Processing

The test setup for this experiment has been introduced previously, in Section 2.2.2. The same six parallel optical fibres (F1-F6) were used in this series of experiments with an average fusion splice to end length of 954 $\pm$ 9 mm. The end of fibre F4, which was identified as anomalous in Section 3.1.2, was re-cut so that the amplitude curve was acceptable. Three reference measurements were taken for each fibre. The temperature in the lab during reference measurements was 22.4 °C. The temperature increased during the data collection process to a final temperature of 23.4 °C.

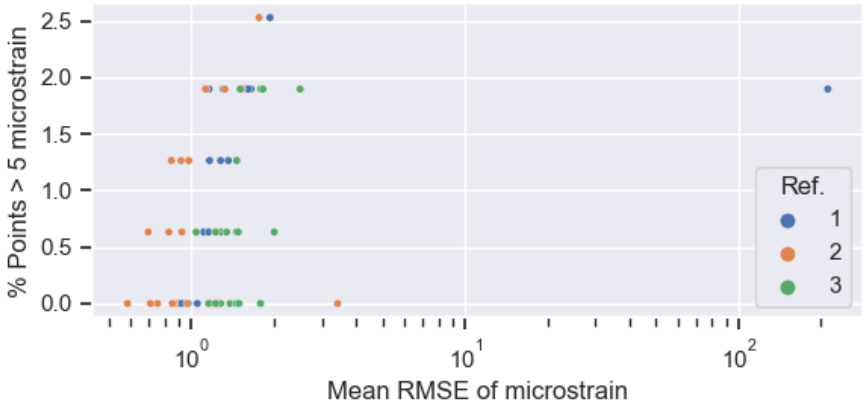

Figure 3.5: Analysis of strain results for fibre F6 in the normal state

Out of three recorded references, the best reference was chosen for each OF. A measurement with a high and sharp end-reflection peak, combined with low levels of noise in the strain measurement was considered to be a good measurement. To analyse the noise level for the *Norm* state (defined in Table 2.2), a text file containing strain data was calculated for each reference dataset. Then, the files were processed to generate statistics such as root mean squared error (RMSE) for the strain values and the percentage of data points > 5 $\mu\epsilon$, which empirically is considered an acceptable level of noise in the strain measurement [20]. Figure 3.5 shows the results for fibre F6, where reference 2 was deemed to perform the best.

Using the least noisy reference for each fibre, a Python script was used to automatically calculate the distributed strain values with the following parameters (defined in Section 2.1.4), giving a total of 159 data points for the selected post-processing parameters:

- sensing range: 800 mm from the splice, excluding the bottom 200 mm in the mesh tube;
- GL: 10 mm;
- SS: 5 mm.

3.2.2 Data Exploration

An example selection of strain curves for fibre F3 is shown in Figure 3.6. The approximate physical location of the transition of the optical fibre from the enclosed tube into the mesh tube is denoted by dashed vertical lines. The general trend is that the strain curves become increasingly noisier (especially with *Fan1-4*) and that the noise propagates from the free fibre end closer to the splice, and even across to the enclosed tube. The plots also show that there are similarities between the disturbed states, for example between *Fan3* and *Fan4*. More examples of strain curves for different levels of disturbances for a similar experiment can be found in [9].

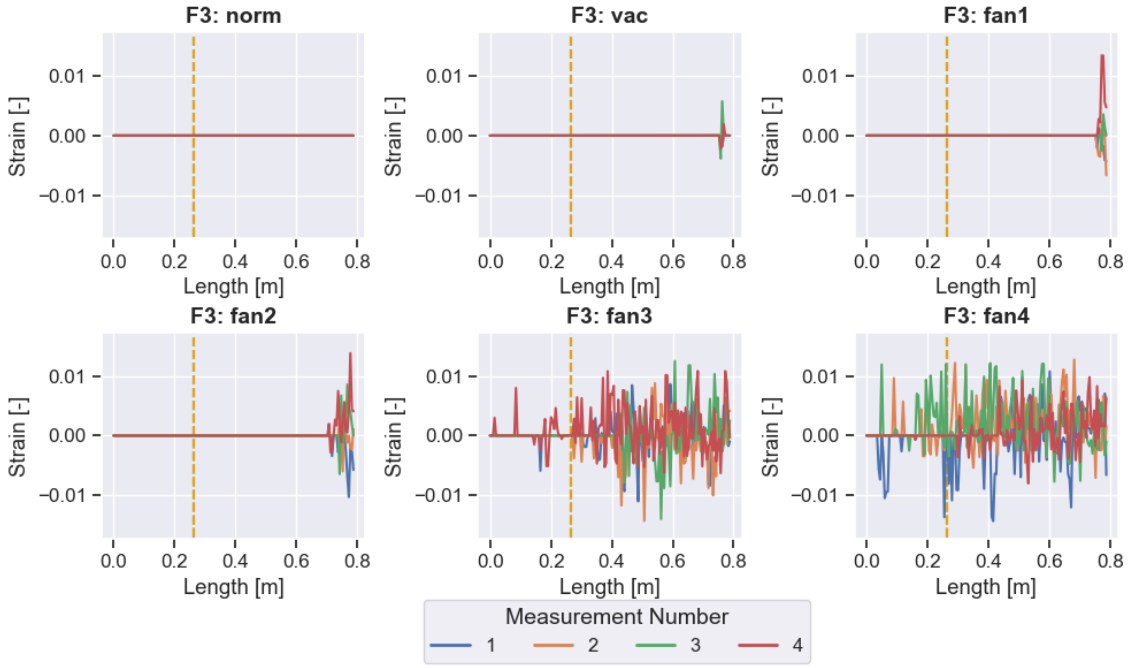

Figure 3.6: Examples of strain curves for fibre F3 during each of the disturbed states (Table 2.2).

A statistical analysis of the strain data revealed some important differences between the measurement states i.e. classes of data. For example, Figure 3.7 shows that the distributions of the strain values along the sensing length can be grouped into three categories according to the probability density function (PDF): the *Norm* state, where most of the strain values are very close to zero, a low-level mechanical disturbance state (*Fan1* or *Vac*) and a high-level mechanical disturbance state (*Fan2-Fan4*). This distinction can also be observed in Figure 3.8, which shows the GADF visualisation for one measurement from each state

for each OF. The *Norm* state has a distinct GADF for all fibres except fibre F5 and the measurements get progressively noisier with increased air fan speed. Additionally, there is some overlap between the states, which can cause confusion for the ANN models. For example, *Fan2-Fan4* are completely different for fibres F1 and F3. Finally, Figure 3.8 also shows that all of the fibre F5 measurements are noisy. Therefore, all the strain data from F5 has been excluded from the training data set of the neural network.

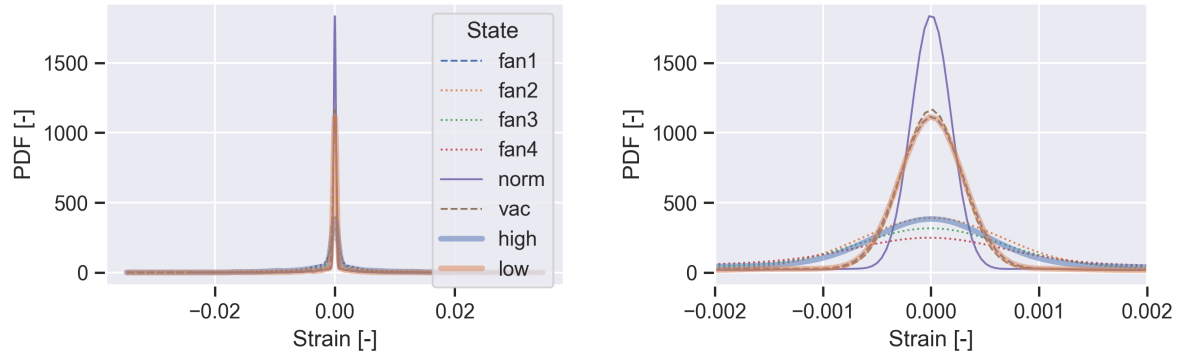

(a) Wide range of strains

(b) Narrow range of strains

Figure 3.7: Distributions of strain values over twenty repeated DOFS measurements (all fibres in different disturbance states).

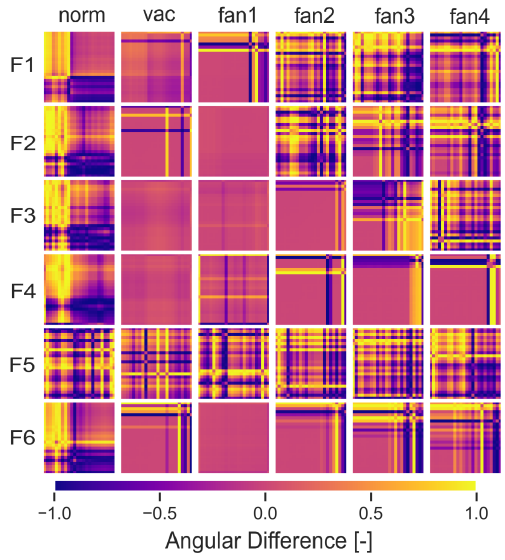

Figure 3.8: GADF visualisations of all fibres (F1-F6) for measurement number 9

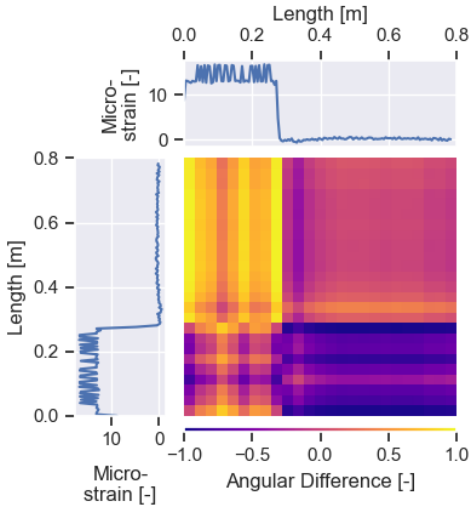

Figure 3.9: Example strain curve and the corresponding GADF for *Norm* state

The transition from the enclosed tube to the steel mesh occurs at approximately 0.26 m from the fusion splice location, as indicated in Figure 2.5 and marked in Figure 3.6. This transition is most prominent in the GADF matrices for the *Norm* state in Figure 3.8 where an abrupt change of colour occurs approximately at the location of the transition. The corresponding strain curve from the *Norm*

state in Figure 3.9 shows that, surprisingly, the part of the OF enclosed in the cardboard tube exhibited higher values of strain than the part in the steel mesh tube.

Figure 3.10 shows FFTs of the audio recordings taken during the disturbance activation on a linear and a logarithmic scale. The trends in the frequency analyses provide more insight into the strain results observed in Figure 3.7. Starting with the *Norm* state, the FFT in Figure 3.10b shows very low levels of background noise. Moving on, the two *Low* group states (*Vac, Fan1*) show slightly higher noise intensities, with *Fan1* having lower intensities than *Vac* across the whole spectrum. It is important to note that *Vac* was perceived to be much louder than any of the *Fan* states, but the microphone picked up the acoustic signal directly from the turbulent air. Ascending up the graph, the audio analysis from *Fan3* and *Fan4* revealed intensities several multitudes higher than the rest of the states. The trends in Figure 3.7 and Figure 3.10 are mostly in accordance with each other: the states with higher and sharper PDF curves had low acoustic intensities across all frequencies, whilst the states with shallow PDF curves (belonging to the *High* group) had high FFT intensities (except for *Fan2*).

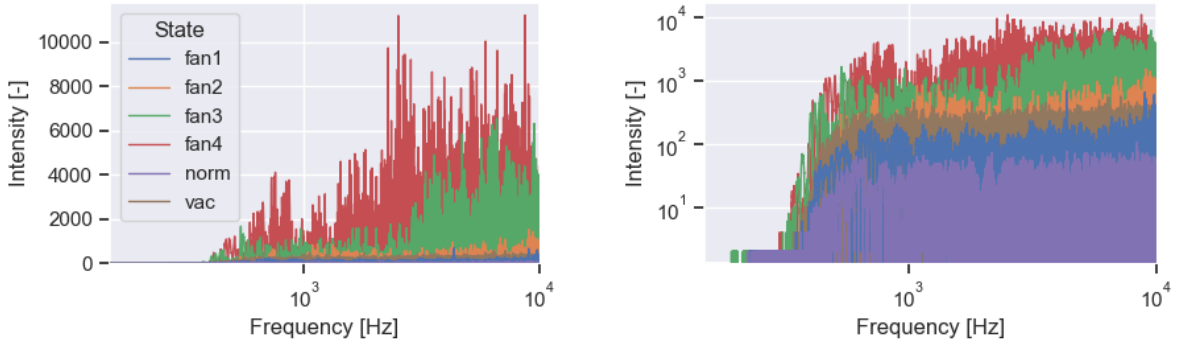

(a) Linear intensity

(b) Log intensity

Figure 3.10: FFT of audio recorded during disturbance activation.

3.2.3 LSTM Predictions

Two LSTM ANNs were developed to classify different vibrational disturbance states that had been applied on the free-hanging optical fibres. The ANN models were developed based on sequential strain data such as shown in Figure 3.6. The training and validation losses for the six-state LSTM ANN are shown in Figure 3.11a, with a minimum training loss of just below 1. Early stopping was invoked at epoch 18 due to the validation loss beginning to increase. The confusion matrix for the first LSTM model (Model LSTM-6), developed by using six pure disturbance classes is shown in Figure 3.11b, where the predictions were made on unseen test data. The labels are organised in ascending acoustic intensity as identified in Figure 3.10b. The fractions of the predictions belonging to each class of data are displayed in the confusion matrix cells.

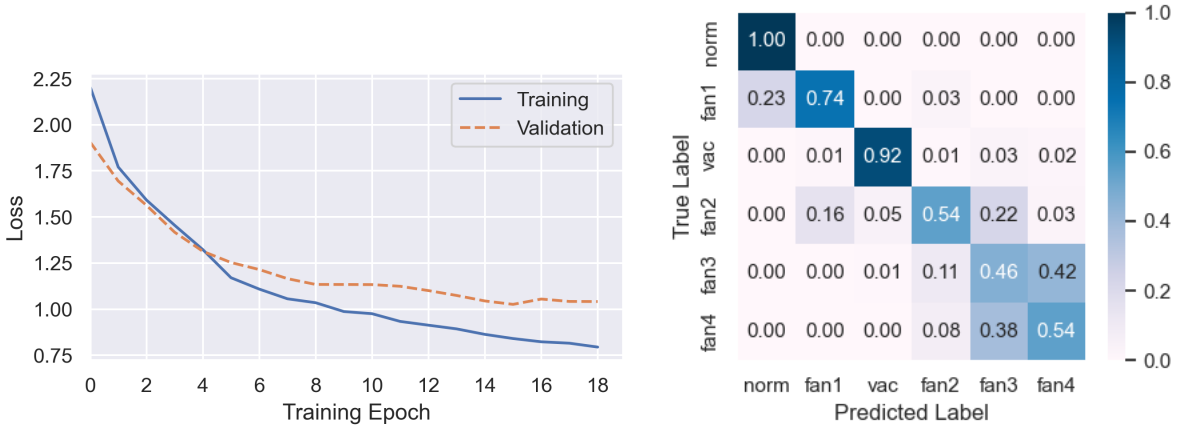

(a) Training and validation loss.

(b) Confusion matrix with an average test prediction accuracy of 70%.

Figure 3.11: Model LSTM-6

Figure 3.12b shows the predictions made by using the second LSTM model (Model LSTM-3) on unseen test data. The disturbance states were grouped into larger classes in accordance with the strain distribution plots in Figure 3.7, also described in Table 2.2. This resulted in a significant increase in the prediction accuracy. Although the loss decrease was less stable during training, a lower minimum loss of approximately 0.38 was achieved, as shown in Figure 3.12a. The training time per epoch with 720 steps was 143 seconds.

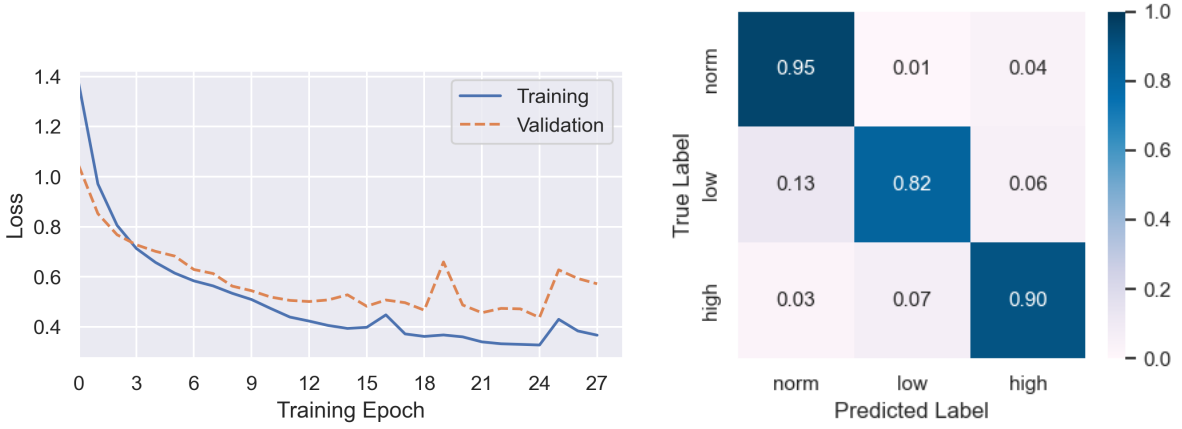

(a) Training and validation loss

(b) Confusion matrix with an average test prediction accuracy of 89%

Figure 3.12: Model LSTM-3 trained on three grouped states

3.2.4 TCN Predictions

As an alternative to the LSTM ANN, a TCN model can be employed for essentially the same numerical task. The results of the predictions made by the TCN network trained on all states (Model TCN-6) are shown in Figure 3.13. The network was trained for 8 epochs before early stopping was activated.

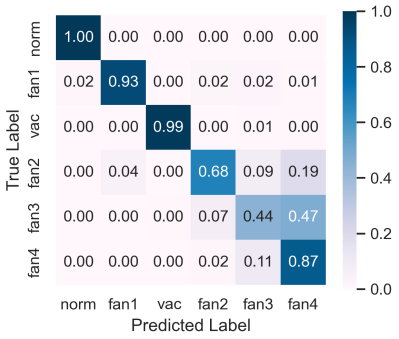

(a) Training set (82%)

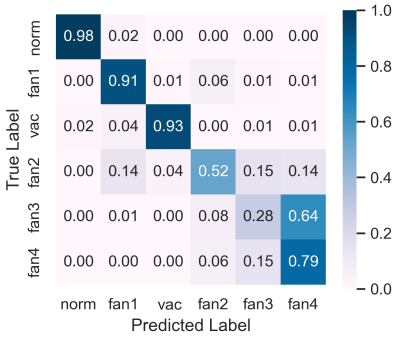

(b) Validation set (74%)

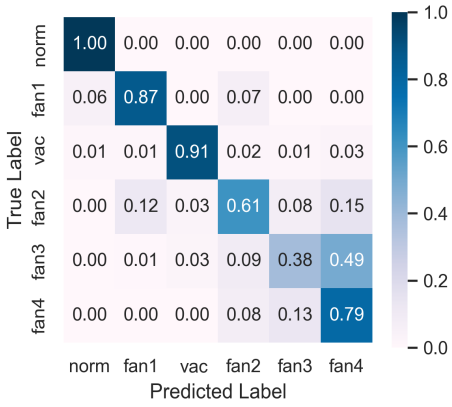

(c) Test set (76%)

Figure 3.13: Predictions made by Model TCN-6 with average prediction accuracy for each data set.

The disturbance states used in Model TCN-3 were grouped into three larger composite classes in the same way as for Model LSTM-3 previously. Similar to the LSTM networks, the TCN performed much better with fewer classes of data. The training time per epoch with 720 steps was however, only 29 seconds.

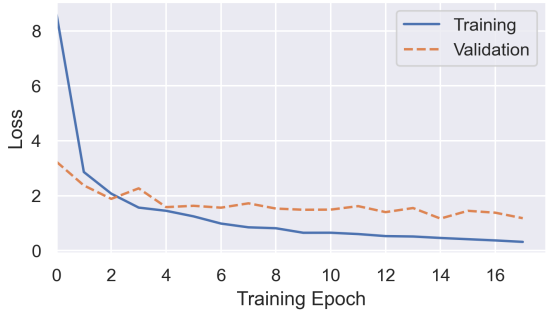

(a) Training and validation loss

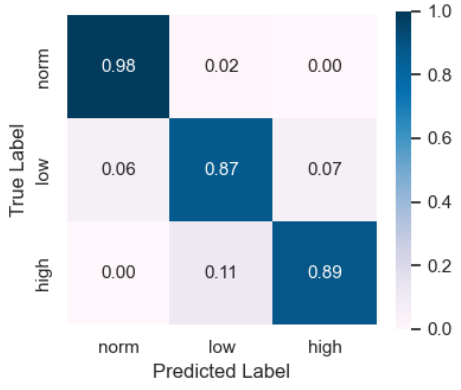

(b) Confusion matrix showing an average prediction accuracy of 84%

Figure 3.14: Model TCN-3 performance (grouped states)

The performances of all four developed ANN models are summarised in Table 3.2.

Table 3.2: Summary of ANN model prediction accuracy

	Data set		
Model	Training	Validation	Test
LSTM-6	76%	70%	70%
TCN-6	82%	74%	76%
LSTM-3	90%	88%	89%
TCN-3	95%	92%	91%

3.2.5 Visual Findings

Some of the video findings from the free-fibre experiments are shown in Figure 3.15, where composite images were generated by stacking up all of the frames in each video and taking the average of these frames. Solid blue lines indicate that the fibres were almost still, such as in the *Norm* state, whilst blurry lines indicate that the fibres moved a lot during the video recording process. As expected, the fibres moved intensely with increasing fan speeds. There were also small movements present during the *Norm* state.

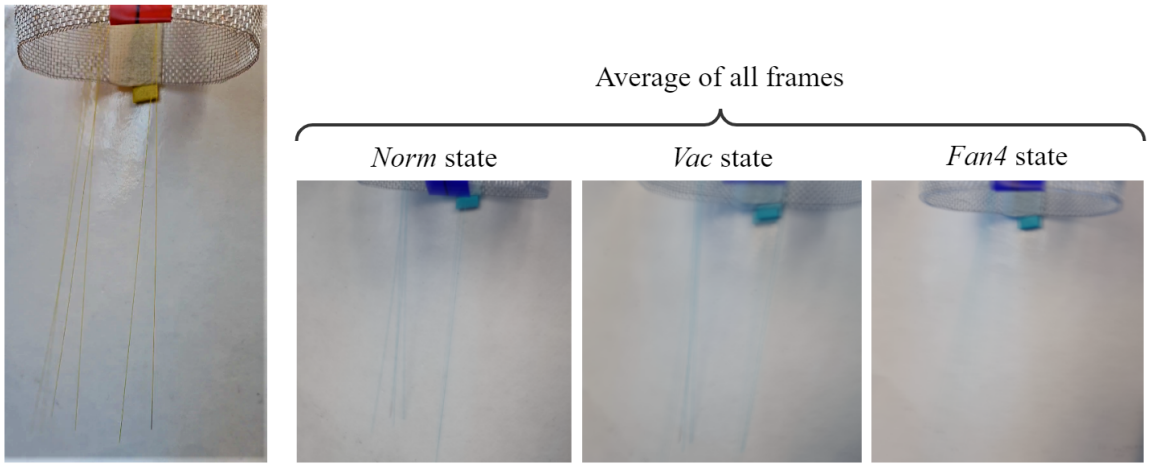

Figure 3.15: Visual motion of fibres in different disturbance states

3.2.6 Discussion

The statistical analysis confirmed that strain curves become progressively noisier with increased intensities of ambient vibrational disturbances. It also showed that some disturbance states, although from very different sources (*Vac, Fan1*), cause a similar response in the strain curves. Plotting the GADF matrices for the measurements was also a useful tool to visualise time-series data and quickly identify the anomalous fibre F5.

The transition between the enclosed cardboard tube and the open steel mesh was easiest to identify in the GADF matrices for the *Norm* state, appearing as two areas of constant colour in the first column of Figure 3.8. It was surprising that strain values were higher for the OF part enclosed in the tube (Figure 3.9). The difference of ca. 10 με between the enclosed cardboard tube strains and the open steel

mesh tube strains can be caused by a temperature gradient. That is, when room temperature shifts by ca. 1 °C from the baseline, artificial strains of ca. 10 με are created in the measurement (due to refractive index change in glass) [25]. The DOFSs inside the enclosed tube always follow the small localised changes in room temperature with a delay.

One parameter which gave a significant performance increase for all ANN models was dropout. Without dropout, the networks would become severely overfitted with an extremely low training loss and a high and unstable validation loss. This was confirmed in numerical trials. Adding dropout increased the training loss, however, it also led to a significant decrease in validation loss and an increase in the test accuracy, meaning the network became more generalised. Other regularisation techniques such as L1- and L2- regularisation for the LSTM networks also helped to generalise the models. For the TCNs, layer normalisation gave an accuracy increase of approximately 5-10% for Model TCN-6 but had a negative effect on Model TCN-3.

Both LSTM models were able to classify disturbance states to some degree. The training, validation and test accuracies in Table 3.2 for the LSTM models were within a range of 6%, suggesting that the model generalised fairly well but may still be slightly overfit. The states in the 6×6 confusion matrices are ordered in increasing degrees of disturbance according to the FFT analysis in Figure 3.10. Although the six-state LSTM-6 model predicted the correct class only 70% of the time, the diagonal trend in Figure 3.11b shows that the model often incorrectly predicted one of the adjacent states. Accounting for this, 94% of the model's predictions were correct within the neighbourhood of one state. The clusters of confusion in the confusion matrix show that the model had trouble differentiating the *Fan2-Fan4* states. Considering the similarities in the GADF matrix textures in Figure 3.8 and also in the video recordings, it is understandable that the model struggled to classify these states correctly. Nevertheless, this numerical analysis shows that the ANN is capable of identifying high and low disturbance states.

It follows that the model with composite states (Model LSTM-3) had a significantly higher overall prediction accuracy than Model LSTM-6. Both models had the same structure but Model LSTM-3 was trained on a dataset consisting of grouped states. Figure 3.12b shows that the grouped model struggled the most with the *Low* disturbance state. This can be attributed to large variations in the *Low* class states with some strain series exhibiting strains similar to the normal threshold and some sharing similarities with *Fan2*, for example.

The TCN models made predictions with a similar test accuracy as their LSTM equivalents. Model TCN-6 nearly always predicted the adjacent state when predicting the incorrect class. In this case, 91% of the predictions in Figure 3.13c would be accurate, with the most problematic state being *Fan3*. The predictions made by Model TCN-3 were similar to that of Model LSTM-3. However, the biggest difference is the training time per epoch: the TCN was five times quicker to train.

The visual findings confirmed that fibres moved more vigorously with increasing the fan speed and that it was difficult to separate states based purely on visual data.

3.2.7 Effect of Virtual Gauge Length Size

After the physical experiment, a numerical parametric study was conducted with six different virtual gauge lengths from 5 mm to 50 mm, constrained to SS = $\frac{1}{2}$GL. Strain curves were generated from the same reference and measurement OBR files but with different post-processing parameters as exemplified in Figure 3.16. The general trend is that strain curves are noisier for smaller gauge lengths. This is

expected because the strain values are averaged over smaller spatial increments, so the noise manifests itself on a smaller scale.

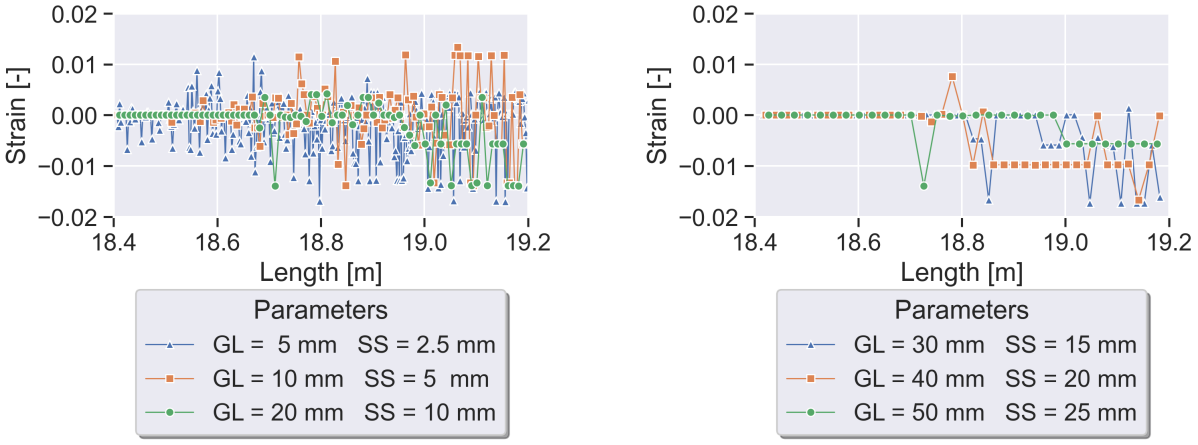

(a) Small virtual gauges

(b) Large virtual gauges

Figure 3.16: Comparison of the same strain measurement re-calculated with various post-processing parameters, GL and SS, using an example curve from the *Fan4* state.

The models were retrained using strain data files generated with new GL and SS parameters. Having changed the post-processing parameters, the data files were of different lengths varying from 31 data points for the largest GL to 325 data files for the smallest GL value. Figure 3.17 shows that the predictive capabilities of both LSTM models remain relatively stable for GL $>$ 10 mm. However, on the whole, the prediction accuracy becomes significantly worse for the smallest gauge length of 5 mm. This is presumably because the curves become excessively noisy for the smallest gauge length as shown in Figure 3.16a. The TCN models reacted differently. Model TCN-6 remained relatively stable, whilst Model TCN-3 showed severe performance degradation for some gauge lengths.

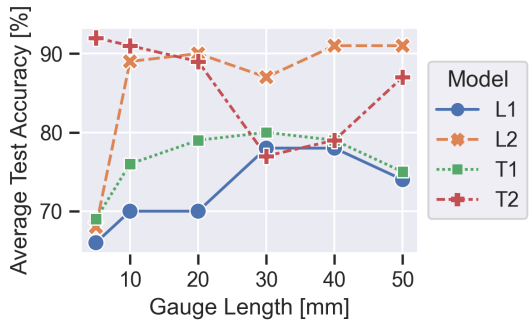

Figure 3.17: The effect of gauge length on prediction accuracy of each ANN model.

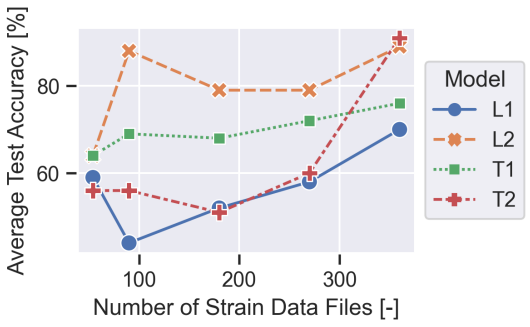

Figure 3.18: The effect of training data quantity on prediction accuracy.

It is worth noting that none of the models were optimised for the new sequence length inputs, which means that performance could be further improved with proper tuning of hyperparameters and a more appropriate network structure. For example, the TCN receptive field size was always 187. This would cause the model to ignore parts of a data series longer than this size. For sequences shorter than this, the sequence would be padded with zeros whilst the information at the end of the sequence, containing the actual strain data, would be diluted due to convolutions.

3.2.8 Effect of Data Set Size

Another numerical study was conducted by training the networks with the original sensing parameters however, with different quantities of training data. The total number of files used for training was 360: 60% of 20 strain files $\times$ 6 states $\times$ 5 fibres. A pseudorandom sub-selection of files was chosen, ensuring that each disturbance class was represented evenly. As expected, Figure 3.18 shows a positive correlation between the number of strain data files used for training and the average test accuracy. It is important to note that the curves in Figure 3.18 have not started to plateau, which suggests that more data files (beyond the current 20 repeated measurements) could further improve the network performance. The use of random number generators introduces stochastic variation to the result. For smaller data batches, the results are more uncertain because the specific selection of randomly-selected files would have a greater effect on the result. The same random seed was used throughout the experimental work, however, using a different random seed could give different results.

3.2.9 Main Takeaways

Both LSTM and TCN structures are capable of differentiating between different modes of vibrational disturbances. Both models' predictions were accurate 70% and 76% of the time, however, they predicted the outcome within one adjacent state neighbourhood over 90% of the time. Although the LSTM and TCN models showed a similar prediction calibre, the TCN was significantly quicker to train which makes it a better choice from a scalability perspective. The numerical parametric study concerning the gauge length revealed that the LSTM networks were largely insensitive to changes in the gauge length above a threshold of 10 mm. Another significant advantage of the TCN structure is that it can process sequences of different lengths, whilst the LSTM input sequence lengths are set based on the sequence lengths of the training series. Therefore the TCN offers more parametric flexibility.

3.3 Classification of Acoustic Vibrations for DOFS Bonded to a Structure

Thus far, free-hanging optical fibres have been considered for vibration classification purposes. However, in most real-life situations optical fibres are attached to a host structure. Therefore, an experiment was conducted to evaluate how acoustic vibration classification is affected when the first eigenfrequency of a structure is activated. External periodic excitation tends to guide a large part of its driving energy towards the lowest vibration mode of the structure. When excited near the fundamental eigenfrequency, a large part of external energy is therefore converted to the mechanical vibrations of the beam. First, the flexural eigenfrequency of the host beam was calculated to establish the target acoustic vibration range. Then, data was collected from a DOFS bonded to a long composite beam and was analysed by two TCN models. The test setup for the bonded DOFS experiment has been described earlier in Section 2.2.2.

3.3.1 Eigenfrequency Calculations

A three-point bending test was first performed to establish the Young's modulus for the long composite beam. The beam was made of $\pm 45°$ glass fibre fabric in an epoxy matrix with an approximate fibre volume fraction of 0.31. The results of the bending test are plotted with a fitted line in Figure 3.19. The Young's modulus was calculated to be 14.6 GPa using Equation 1 with the beam parameters in Table 2.3. The first flexural eigenfrequency for the long beam was calculated to be 58 Hz using Equation 2. To study near-resonance DOFS performance, the acoustic experiments were performed over a frequency range of [48, 68] Hz in increments of 1 Hz. This was done for three volume levels on the PC: 25%, 50% and 75% of the maximum speaker volume.

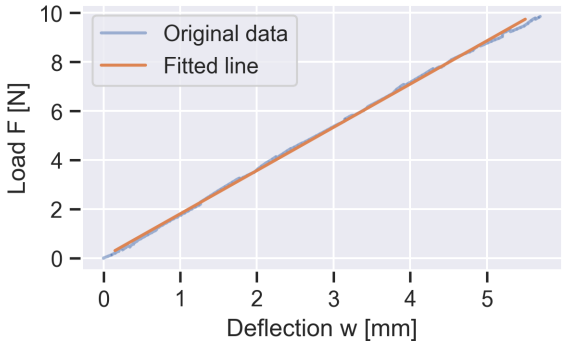

Figure 3.19: Load-deflection curve from a three-point bending test.

3.3.2 Data Exploration

To get an overview of experimentally measured strains, strain curves were visualised for all frequencies and volumes and can be viewed in Appendix A. The DOFS strain measurements were observed to exhibit three different trends: low to moderate levels of noisy strains for frequencies in the range [48, 56] Hz, discrete strain spikes at ca. 0.55 m for frequencies in the range [57, 62] Hz and high noise levels for the range [63, 67] Hz. These trends were most prominent at the intermediate speaker volume of 50% maximum. To exemplify the three main strain patterns, selected strain curves for three different frequencies are shown in Figure 3.20. The dashed vertical lines denote the range of positions where the OF is fixed to the specimen.

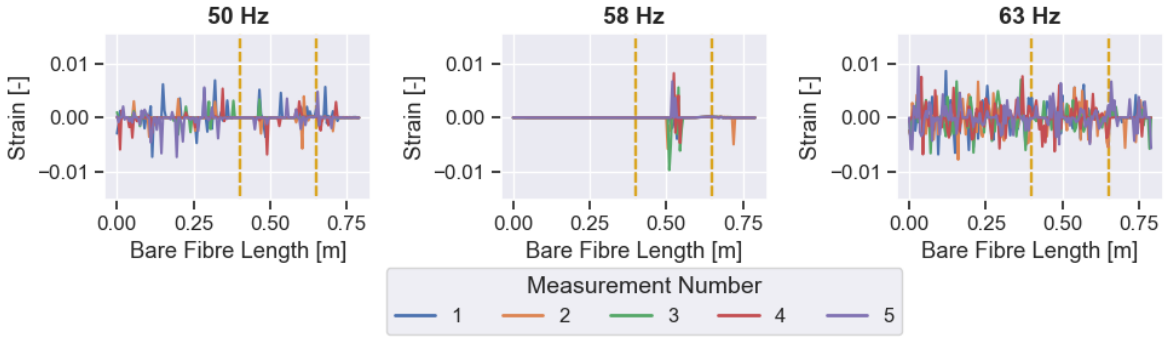

Figure 3.20: Five arbitrarily chosen measurements at three selected frequencies excited at 50% maximum volume.

Figure 3.21 shows the PDF for the spectrum of tones played by the speaker for the 75% volume level. The tones presumably closest to the eigenfrequency of the composite beam are in the middle of the spectrum. At first glance, it appears that tones on the lower end of the activated frequency spectrum cause lower strain values than tones on the higher end, due to their high PDF peaks. However, the FFT of the speaker output in Figure 3.22 reveals that the speaker output did not have a constant amplitude across the whole frequency spectrum, despite volume dials being kept constant. This could be the reason behind the trend in the PDF plot - the strain data is noisier (i.e. has more variation) for higher frequencies due to the higher excitation amplitude for those frequencies.

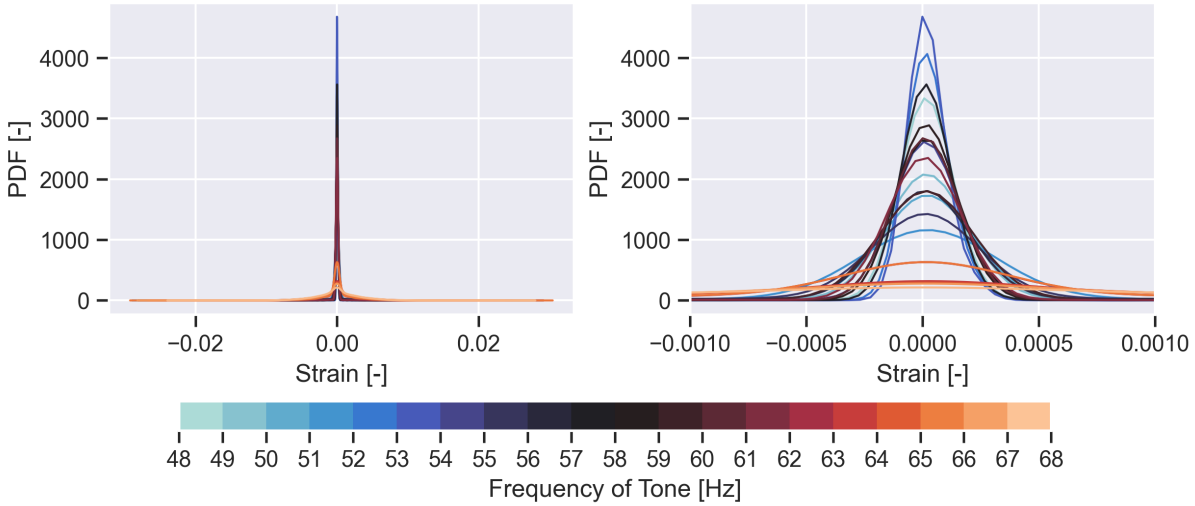

Figure 3.21: Distribution of strain values for each acoustic tone for 75% volume level.

Figure 3.22 also shows that the tones from the speaker are not pure, but rather accompanied by harmonics, characterised by the repeating peak groups in the plot to the left. Zooming in on the fundamental frequency range in the FFT plot (figure on the right) confirms that the most prominent tones played by the speaker were in fact the programmed tones.

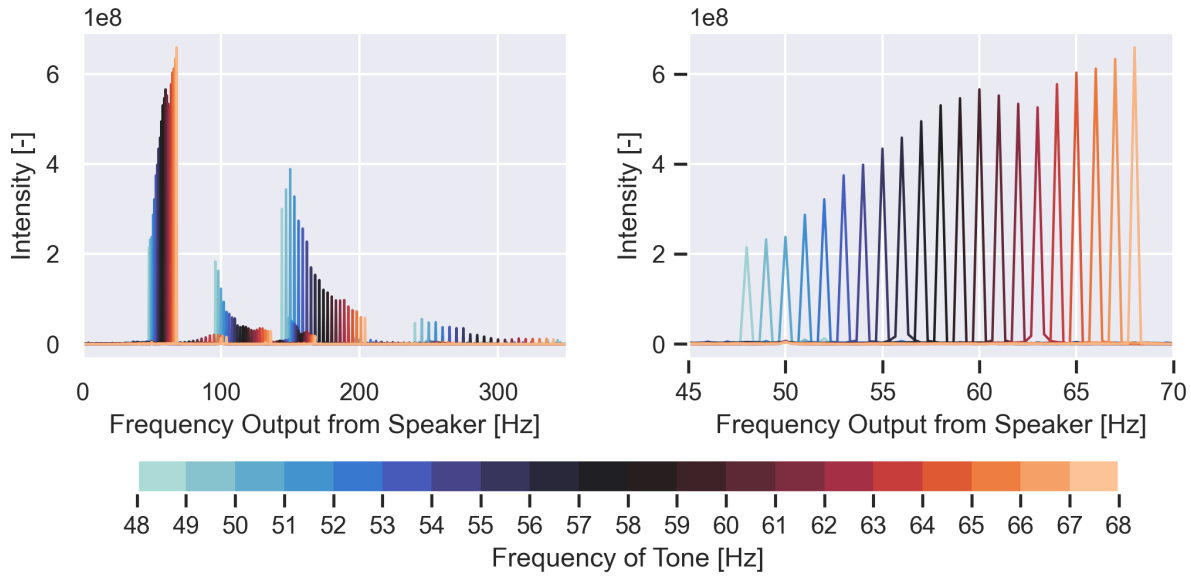

Figure 3.22: Fourier transforms of 21 discrete tones played by the speaker and recorded by the mic, plotted on the same axes for comparison.

To establish an overview of possible systematic variations in DOFS strains, GADF matrices for the first ten strain measurements for each frequency played at a volume level of 50% are displayed in Figure 3.23. It is very difficult to see any clear correlation between the frequency and the GADF matrix texture. For each considered frequency, and across ten repeated experiments, there are some measurements with a few spikes of strain, which produce GADF matrices with constant colour. At the same time, there are some noisy measurements which produce chequered patterns. There is a high variation in response to what should be identical repeated experiments. Across the frequencies, the higher end of the spectrum ($>$62 Hz) tends to have a higher number of noisy strain measurements. This can be explained by variations in excitation amplitudes, as discussed with Figure 3.21 and Figure 3.22 previously.

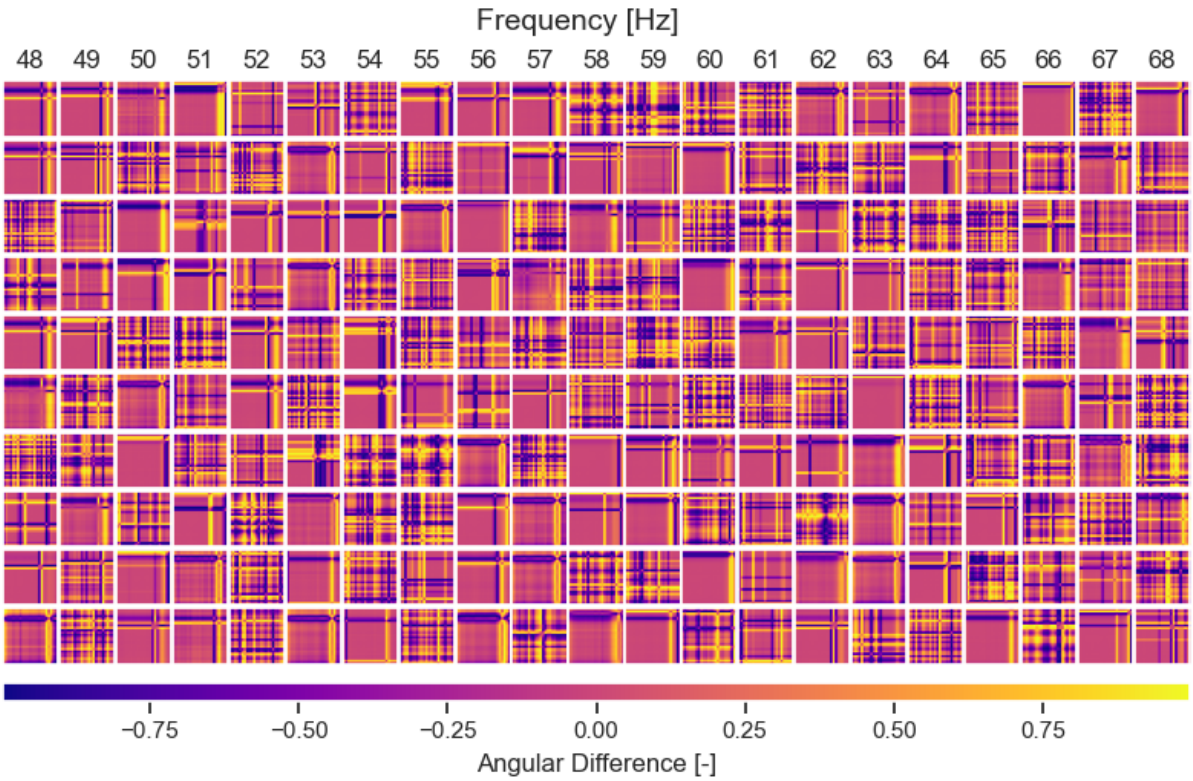

Figure 3.23: GADF matrix textures for the first ten strain measurements (vertical direction) taken for the same volume level (50%) for each discrete frequency.

3.3.3 Categorical TCN Predictions

For bonded DOFS experiments, only the better-performing TCN models were constructed (as defined in Table 2.9). Trained TCN classification models were created for each individual data set corresponding to a specific volume level and a mixture of these data sets. The first network was trained to predict at the same 1 Hz frequency resolution as the data set. The confusion matrix for a TCN model trained on 50% volume level is shown in Figure 3.24. The expected natural frequency of 58 Hz does not appear distinct from other frequencies of the data set. Clusters of confusion appeared amongst neighbouring frequencies, therefore, TCN networks were also trained with grouped states. A confusion matrix from one of the grouped states with a prediction resolution of 4-5 Hz is shown in Figure 3.25. The test accuracy improved from 55% to 84%. Similar to experiments with free-hanging optical fibres, grouped states will naturally diminish in data resolution, whilst gaining significantly in the prediction accuracy.

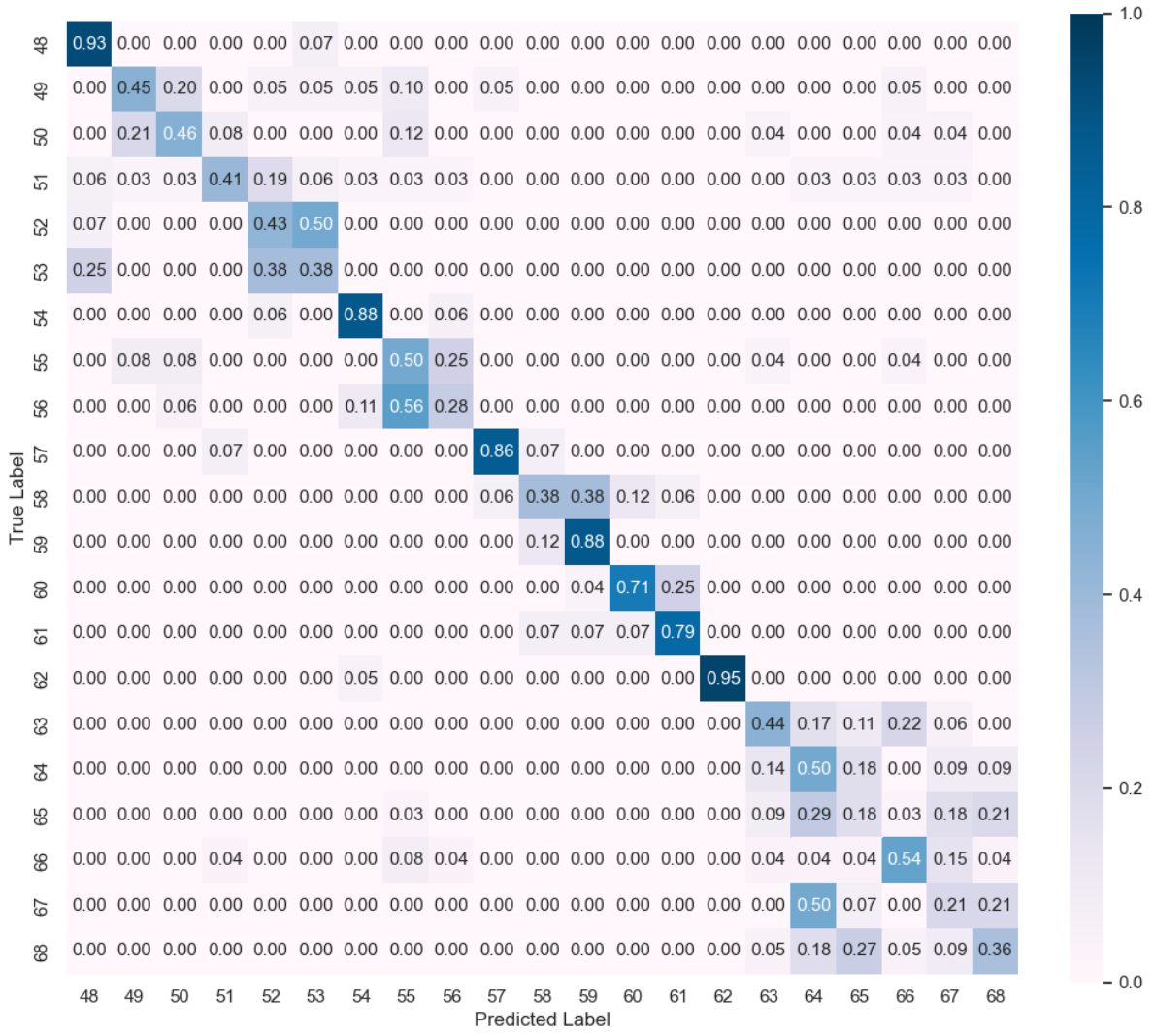

Figure 3.24: Confusion matrix for frequency classification task. Data is gathered at 50% maximum speaker volume, for discrete frequency increments of 1 Hz. Average test accuracy: 55%.

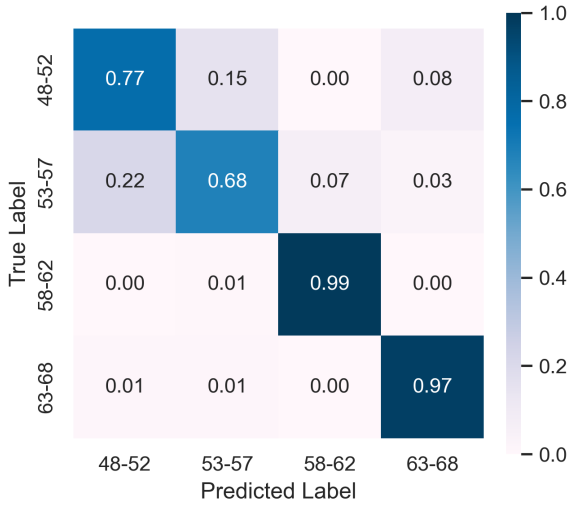

Figure 3.25: Confusion matrix for grouped frequency range classification. Data is gathered at 50% maximum speaker volume, for frequency intervals over 4-5 Hz of discrete values. Average test accuracy: 85%.

3.3.4 Prediction Accuracy and Frequency Resolution

The choice of presenting the confusion matrix only for the 4-5 Hz group (Figure 3.25) is arbitrary. A parametric study was conducted to compare the TCN prediction accuracy for five different frequency resolutions. Figure 3.26 shows a comparison of different grouped data sets for each model. The prediction resolution is defined as the group size for each prediction class and ranged from 1 Hz (21 individual frequencies) to 10 Hz (two frequency groups of 48-58 Hz and 59-68 Hz). From Figure 3.26, it appears that the prediction accuracies of all data sets converge when the prediction resolution is larger. This is expected because the prediction accuracy for only one class would always be 100%. The training accuracy remains fairly stable and high across the prediction resolution range, however, the validation and test accuracy increase significantly as the resolution group increases. A high discrepancy between training and validation/test accuracies is generally a sign of overfitting. To mitigate overfitting, a high dropout rate of 0.3 was used, as well as early stopping.

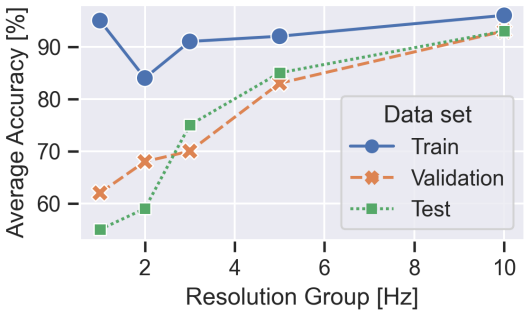

Figure 3.26: Comparison of prediction capabilities for different grouped resolutions.

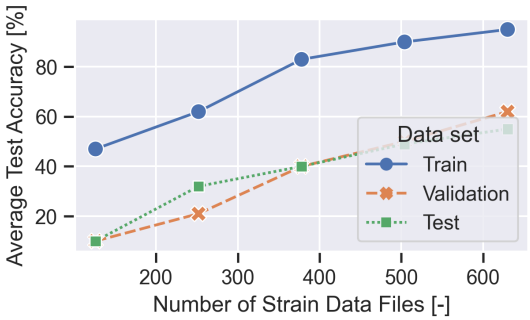

Figure 3.27: The effect of training data quantity on prediction accuracy.

3.3.5 Prediction Accuracy and Training Data Set Size

A convergence study was conducted to investigate whether enough data files were gathered for training and testing the ANNs. The maximum number of files used for training was 630: 60% of 50 repeated measurements/frequency $\times$ 21 frequencies. Figure 3.27 shows that TCN prediction accuracy for all data sets had not converged even with a 630 file data set, and may continue to increase with more files. It also revealed that the difference between the training and validation/test accuracies remained fairly constant.

3.3.6 Continuous TCN Predictions

A different classification philosophy was also considered. A TCN model with only one output neuron, as defined in Table 2.9, was trained to predict a continuous value between the scaled input frequencies. This makes it possible to predict frequencies on a continuous scale rather than over discrete frequencies as considered thus far. Figure 3.28 shows the frequency predictions of the network predictions after upscaling and rounding them to the nearest integer. The size of the markers corresponds to how many data points share the same x- and y-values and the green markers show what the graph would look like if the predictions were identical to the labels. The training, validation and test mean absolute error (MAE) were 1.58 Hz, 2.15 Hz and 2.27 Hz respectively, that is to say, on average, predictions made on unseen data were correct within 2.27 Hz. The corresponding cumulative distribution plot of the absolute error (AE) shows that ca. 20% of the predictions were of the correct class and ca. 95% were correct within 5 Hz.

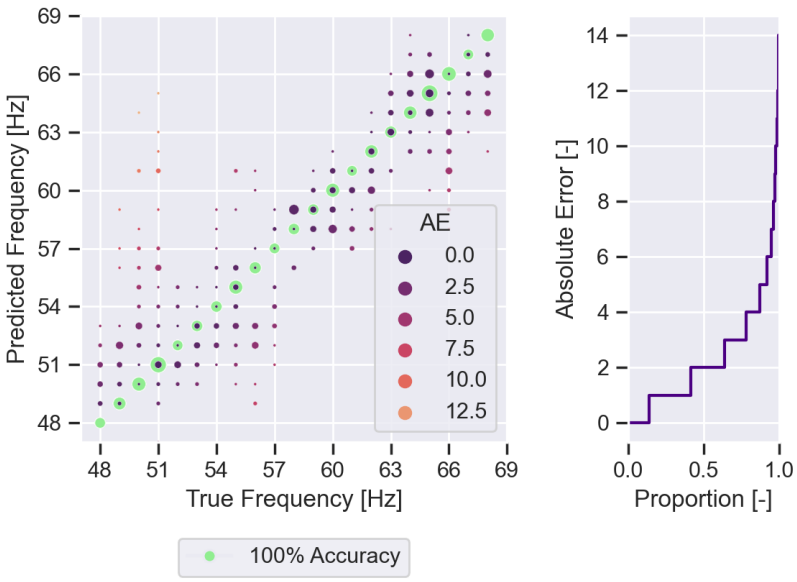

Figure 3.28: Scatter plot of frequency predictions with corresponding cumulative distribution plot displaying an MAE of 2.27 Hz.

Figure 3.29 provides a deeper look into the model predictions for each true frequency. The colour of the box corresponds to the MAE of the predictions for that class. It appears that the model struggled the most with predicting 51 Hz class. However, it predicted 58 Hz, the presumed eigenfrequency class, with the lowest error rate.

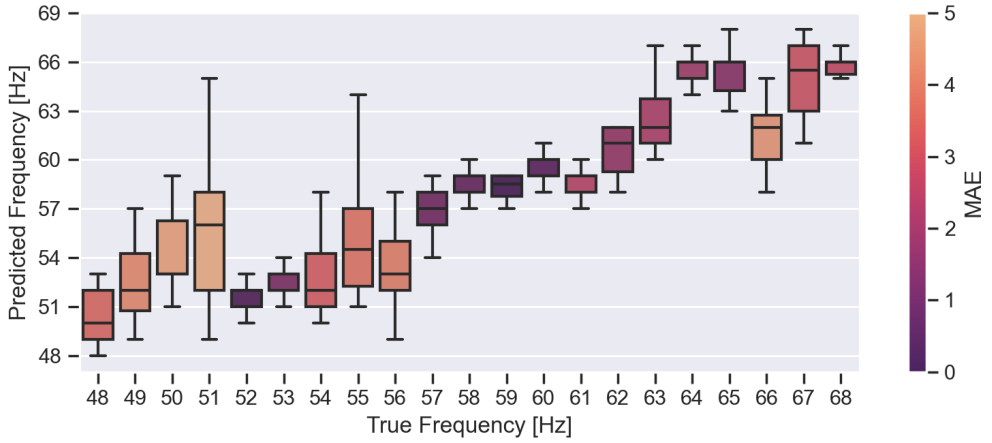

Figure 3.29: Box and whisker plots showing the distribution of the predictions for each 1 Hz frequency.

3.3.7 Discussion

The strain analysis of the acoustically excited free-free beam, with a bonded DOFS, produced very interesting insights. Visualisations of strain measurements revealed that excitation frequencies close to the first flexural eigenfrequency of the beam exhibit strain spikes in the part of the OF that is positioned in the middle of the beam (Figure 3.20). The spikes observed in the strain measurement in the middle of the beam can be interpreted as the manifestation of the antinode in the first flexural mode. Apart from the spike, the strain values for these frequencies were ca. zero. For frequencies outside of this range, the strain curves were noisy, with spikes along the whole length of the embedded fibre. A possible explanation for this could be that when the beam is vibrating off-frequency, the vibrations are more random and uncontrolled, whilst on-frequency, the anti-nodes serve as points of high strain along the fibre.

Similar trends were observed in the data gathered for the other two speaker volumes, but not as clearly as for the intermediate volume (see Appendix A). This could be because the lowest volume was not powerful enough to excite the beam, whilst the highest volume was too powerful and caused excessive movement and noise. Indeed, training the networks on data sets with mixed volume levels gave much worse prediction accuracies and these results were hereby not reported. Although the volume of the speaker was unaltered using the speaker dials, the FFT revealed that the output of the speaker had varying amplitudes for different frequencies. This is presumably because the speaker frequency range is 20 Hz - 200 Hz (only the subwoofer was used), making it more optimised to play frequencies closer to the middle of the range. Similarly, the recorded amplitude difference could be partly attributed to the sensitivity range of the recording device, which is limited to 20 Hz - 20 kHz. To stringently test the effect of sound frequency on strain data from DOFS in structures, the amplitude would have to be kept constant.

Another factor which may have affected the quality of the data is the order in which the OBR scans were performed. The script was programmed to take fifty repeated measurements for a constant tone before advancing to the next frequency, with 48 Hz being the first frequency and 68 Hz being the last. In total, it took approximately 7-8 hours to perform the scans for the whole range of frequencies for one amplitude level. This means that OBR scans taken towards the end of the data collection process could have deviated from the reference files more than the preceding measurements due to temperature changes in the lab, inciting artificially higher strains in the measurement. As mentioned previously, the

temperature can vary by ca. 1-2 °C in the lab throughout the day. A randomised implementation, where the script iterates through the frequency spectrum for a given number of measurements, could be a better solution so that the measurements affected by a temperature difference are represented in each frequency class.

It was possible to train TCNs to predict the frequency of the acoustic disturbance to some degree. Although the parametric study revealed that the models with small prediction ranges had relatively low test accuracies, it is possible to achieve test accuracies of over 80% for prediction ranges larger than 5 Hz. Some inherent prediction error should be expected when the frequency groups are created in such a way. This is because the frequencies that are on the edge of their respective group range may be more similar to a neighbouring frequency belonging to a different group, rather than those in its assigned group. For example, with reference to Figure 3.25, 57 Hz, which is placed in the 53-57 Hz group is likely to be similar to 58 Hz, which belongs to the adjacent group. For this inherent drawback of discrete classification, a TCN making one continuous prediction was also trialled, where the evaluation metric was mean absolute error (MAE). Using this network structure, approximately 40% of predictions were correct within a 1 Hz range, which is 15% lower than from the categorical TCN for the same resolution. For a resolution range of 5 Hz, 95% were correct using the continuous TCN. Comparable results can be seen for the categorical TCN from the clusters of confusion in the 21×21 confusion matrix in Figure 3.24 and the 4×4 confusion matrix in Figure 3.25.

When using the categorical TCN, the frequency labels are treated as individual and unrelated categories. When using the continuous TCN, the frequency categories are treated as though they are related, which is the physical reality. It is difficult to establish whether the frequency should have been treated as a categorical or a continuous variable in this case because both approaches performed well.

4 Conclusions

A series of experiments were conducted to investigate the effects of vibrational disturbances on DOFS strain data measurements. Starting with the tip-termination analysis, an end-reflection length was established based on a statistical analysis of raw amplitude data. The analysis revealed that data from the last 150 mm of the DOFS end contains a strong reflection effect and should be disregarded. However, there is a large variation between different physical OFs depending on how the fibre is actually cut.

Using the free-hanging fibres as the experimental set-up, it was shown that vibrational noise manifests itself in the form of abnormally high strain values in DOFS measurements, even in the absence of exerted mechanical strain. Higher noise intensities cause a larger proportion of the strain measurement values to take on abnormally large values. For classification of noise, an LSTM model and a TCN were trained on strain data gathered from disturbed free-hanging DOFS. It was possible to differentiate between six states of perturbations with an accuracy of over 70%. Moreover, the models successfully managed to separate states from two very different sources, but with approximately the same intensity, namely the *Fan1* and *Vac* states. Grouping the disturbance states into compound groups further improved the prediction accuracies of both models. Although both the LSTM ANN and TCN exhibited similar prediction accuracies, the TCN was five times quicker to train and can process different sequence lengths with the same model.

The final experiment involved exciting a DOFS bonded to a long composite beam to classify acoustic disturbances in a vibrational range surrounding its first fundamental frequency. No clear correlation could be observed between the frequency and the strain measurement output and it was not possible to isolate the eigenfrequency using a resolution of 1 Hz. Only TCN structures were employed for classification predictions in this task. The networks were trained to predict the frequency of the acoustic disturbance and tested on grouped composite states spanning across several resolutions. A categorical and a continuous TCN structure were trialled for the prediction task, with the categorical network performing better. The highest prediction accuracy for a resolution of 1 Hz was achieved using the categorical network, which was 55%.

To summarise, the analyses hereby presented indicate that ANN models are capable of distinguishing between classes of mechanical and acoustic disturbances separated by both intensity and source. This investigation serves as a proof-of-concept for the use of DOFS for vibration sensing in combination with appropriate numerical tools. This approach shows very good potential for extracting new useful information from vibrational disturbances on DOFSs strains, whose effect has thus far been considered only as noise.

References

[1] Regina Magalhães, João Pereira, Oleksandr Tarasenko, Sonia Martin-Lopez, Miguel González-Herráez, Walter Margulis, and Hugo Fidalgo Martins. Towards Distributed Measurements of Electric Fields Using Optical Fibers: Proposal and Proof-Of-Concept Experiment. *Sensors (Basel, Switzerland)*, 20(16):4461, August 2020.

[2] P. F. Kashaykin, A. L. Tomashuk, S. A. Vasiliev, A. D. Ignatyev, A. A. Shaimerdenov, Yu. V. Ponkratov, T. V. Kulsartov, Y. A. Kenzhin, Sh. Kh. Gizatulin, T. K. Zholdybayev, Y. V. Chikhray, and S. L. Semjonov. Radiation resistance of single-mode optical fibres with view to in-reactor applications. *Nuclear Materials and Energy*, 27:100981, June 2021.

[3] Wolfgang R. Habel and Katerina Krebber. Fiber-optic sensor applications in civil and geotechnical engineering. *Photonic Sensors*, 1(3):268–280, September 2011.

[4] Daniel Peairs, Lisa Sterner, Kevin Flanagan, and Vladimir Kochergin. Fiber Optic Monitoring of Structural Composites using Optical Backscatter Reflectometry. *Luna Innovations Incorporated*, January 2009.

[5] Yi Bao, Mahdi Valipour, Weina Meng, Kamal H. Khayat, and Genda Chen. Distributed fiber optic sensor-enhanced detection and prediction of shrinkage-induced delamination of ultra-high-performance concrete overlay. *Smart Materials and Structures*, 26(8):085009, July 2017. Publisher: IOP Publishing.

[6] Shaoquan Wang, Kaspar Lasn, Christer Westum Elverum, Di Wan, and Andreas Echtermeyer. Novel in-situ residual strain measurements in additive manufacturing specimens by using the Optical Backscatter Reflectometry. *Additive Manufacturing*, 2020.

[7] J. M. Muggleton, R. Hunt, E. Rustighi, G. Lees, and A. Pearce. Gas pipeline leak noise measurements using optical fibre distributed acoustic sensing. *Journal of Natural Gas Science and Engineering*, 78:103293, June 2020.

[8] Chris Vallance. Subsea internet cables could help detect earthquakes. `https://www.bbc.com/news/technology-61506705`, May 2022.

[9] Valeria Usenco. Machine learning methods to analyse compromised DOFS data, 2021. Unpublished. Available on request.

[10] Junchan Li, Yu Wang, Pengfei Wang, Qing Bai, Yan Gao, Hongjuan Zhang, and Baoquan Jin. Pattern Recognition for Distributed Optical Fiber Vibration Sensing: A Review. *IEEE Sensors Journal*, 21(10):11983–11998, May 2021. Conference Name: IEEE Sensors Journal.

[11] Yu Bai, Jichuan Xing, Fei Xie, Sujie Liu, and Jinxin Li. Detection and identification of external intrusion signals from 33km optical fiber sensing system based on deep learning. *Optical Fiber Technology*, 53:102060, December 2019.

[12] Huijuan Wu, Ya Qian, Wei Zhang, and Chenghao Tang. Feature extraction and identification in distributed optical-fiber vibration sensing system for oil pipeline safety monitoring. *Photonic Sensors*, 7(4):305–310, December 2017.

[13] Gong-Yu Hou, Zi-Xiang Li, Kai-Di Wang, and Jin-Xin Hu. Structural Deformation Sensing Based on Distributed Optical Fiber Monitoring Technology and Neural Network. *KSCE Journal of Civil Engineering*, 25(11):4304–4313, November 2021.

[14] Chengang Lyu, Ziqiang Huo, Xin Cheng, Jianying Jiang, Alimina Alimasi, and Hongchen Liu. Distributed Optical Fiber Sensing Intrusion Pattern Recognition Based on GAF and CNN. *Journal of Lightwave Technology*, 38(15):4174–4182, August 2020.

[15] Seedahmed S. Mahmoud and Jim Katsifolis. Robust event classification for a fiber optic perimeter intrusion detection system using level crossing features and artificial neural networks. In *Fiber Optic Sensors and Applications VII*, volume 7677, pages 60–71. SPIE, April 2010.

[16] T. H. Loutas, A. Panopoulou, D. Roulias, and V. Kostopoulos. Intelligent health monitoring of aerospace composite structures based on dynamic strain measurements. *Expert Systems with Applications*, 39(9):8412–8422, July 2012.

[17] Linh V. Nguyen, Cuong C. Nguyen, Gustavo Carneiro, Heike Ebendorff-Heidepriem, Heike Ebendorff-Heidepriem, Stephen C. Warren-Smith, Stephen C. Warren-Smith, and Stephen C. Warren-Smith. Sensing in the presence of strong noise by deep learning of dynamic multimode fiber interference. *Photonics Research*, 9(4):B109–B118, April 2021.

[18] ClearLite ® POLY 1550 17 Optical Fiber. `https://fiber-optic-catalog.ofsoptics.com/documents/pdf/BF06158-02-Clearlite-POLY-1550-17-Optical-Fiber-web.pdf`. Accessed: 05-02-2022.

[19] Søren Heinze. OBR-Running-Reference-Method-Software. `https://github.com/SorenHeinze/OBR-Running-Reference-Method-Software`, 2018. Accessed: 29-01-2022.

[20] Erik Saeter, Kaspar Lasn, Fabien Nony, and Andreas T. Echtermeyer. Embedded optical fibres for monitoring pressurization and impact of filament wound cylinders. *Composite Structures*, 210:608–617, February 2019.

[21] Optical Backscatter Reflectometer 4600 User Guide. `https://lunainc.com/sites/default/files/assets/files/resource-library/OBR-4600-UG6_SW3.10.1.pdf`. Accessed: 05-02-2022.

[22] D. Gloge, P. W. Smith, D. L. Bisbee, and E. L. Chinnock. Optical fiber end preparation for low-loss splices. *The Bell System Technical Journal*, 52(9):1579–1588, November 1973.

[23] Delta AFB $90 \times 90 \times 24.4$ mm. `https://datasheetspdf.com/pdf-file/805057/DELTA/AFB0912VH/1`. Accessed: 08-02-2022.

[24] Foxconn PV903212PSPF Server - Square Fan 0A, sq $90 \times 90 \times 32$. `https://www.elecok.com/no/data_sheet/162055/FOXCONN_PV903212PSPF_0A_12V_0%2C60A_4wires_kj%C3%B8ling_fan_(NO).pdf`. Accessed: 08-02-2022.

[25] Shaoquan Wang and Kaspar Lasn. Accurate non-linear calculation model for decoupling thermal and mechanical loading effects in the OBR measurements. *Optics Express*, 29(2):1532, January 2021.

[26] ASTM International Standard E1876-09. Standard test method for dynamic Young's modulus, shear modulus, and Poisson's ratio by sonic resonance, 2013.

[27] Philippe Remy. Temporal convolutional networks for keras. `https://github.com/philipperemy/keras-tcn`, 2020.

[28] Johann Faouzi and Hicham Janati. pyts: A python package for time series classification. *Journal of Machine Learning Research*, 21(46):1–6, 2020.

[29] tsaug. `https://github.com/arundo/tsaug`. Accessed: 2022-02-22.

[30] Qingsong Wen, Liang Sun, Fan Yang, Xiaomin Song, Jingkun Gao, Xue Wang, and Huan Xu. Time Series Data Augmentation for Deep Learning: A Survey. *Proceedings of the Thirtieth International Joint Conference on Artificial Intelligence*, pages 4653–4660, August 2021. arXiv: 2002.12478.

[31] Compare the effect of different scalers on data with outliers — scikit-learn 1.0.2 documentation.

[32] Sergey Ioffe and Christian Szegedy. Batch Normalization: Accelerating Deep Network Training by Reducing Internal Covariate Shift. *arXiv:1502.03167 [cs]*, March 2015. arXiv: 1502.03167.

[33] Colin Lea, Michael D. Flynn, Rene Vidal, Austin Reiter, and Gregory D. Hager. Temporal Convolutional Networks for Action Segmentation and Detection. In *2017 IEEE Conference on Computer Vision and Pattern Recognition (CVPR)*, pages 1003–1012, Honolulu, HI, July 2017. IEEE.

[34] Shaojie Bai, J. Zico Kolter, and Vladlen Koltun. An Empirical Evaluation of Generic Convolutional and Recurrent Networks for Sequence Modeling. *arXiv:1803.01271 [cs]*, April 2018. arXiv: 1803.01271.

[35] Aaron van den Oord, Sander Dieleman, Heiga Zen, Karen Simonyan, Oriol Vinyals, Alex Graves, Nal Kalchbrenner, Andrew Senior, and Koray Kavukcuoglu. WaveNet: A Generative Model for Raw Audio. *arXiv:1609.03499 [cs]*, September 2016. arXiv: 1609.03499.

[36] Martin T Hagan, Howard B Demuth, and Mark Beale. *Neural network design*. PWS Publishing Co., 1997.

[37] Zhiguang Wang and Tim Oates. Imaging Time-Series to Improve Classification and Imputation. *arXiv:1506.00327 [cs, stat]*, May 2015. arXiv: 1506.00327.

[38] Valeria Usenco and Kaspar Lasn. Classification of Vibration-Compromised DOFS Data with LSTM Neural Networks. In *The 8th European Congress on Computational Methods in Applied Sciences and Engineering ECCOMAS Congress 2022*, Oslo, Norway, June 2022. (Under review).

Appendices

Appendix A Strain Measurements from DOFS Bonded to a Composite Beam

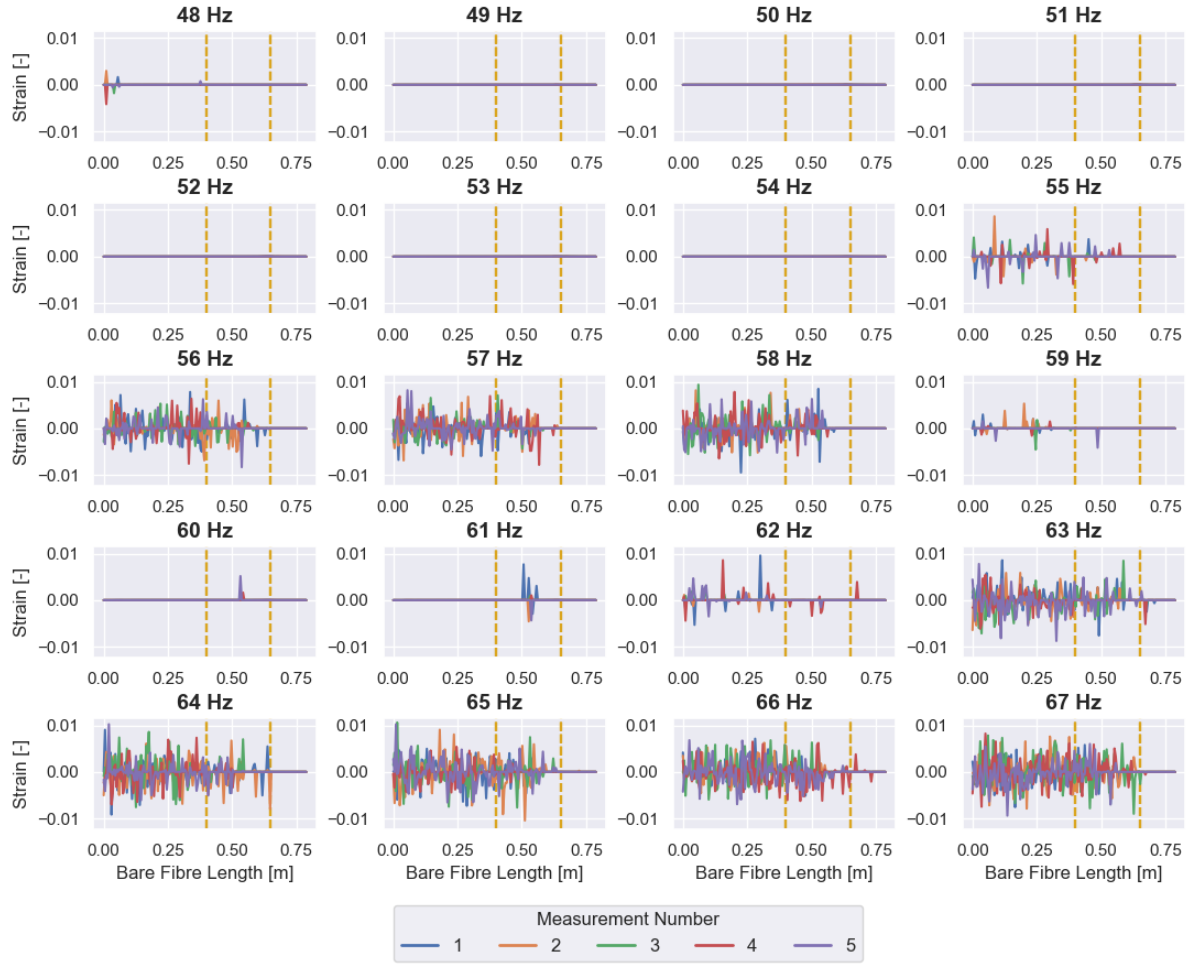

Figure A.1: Strain measurements gathered at 25% maximum volume. The vertical lines mark the section of the DOFS bonded to the composite beam.

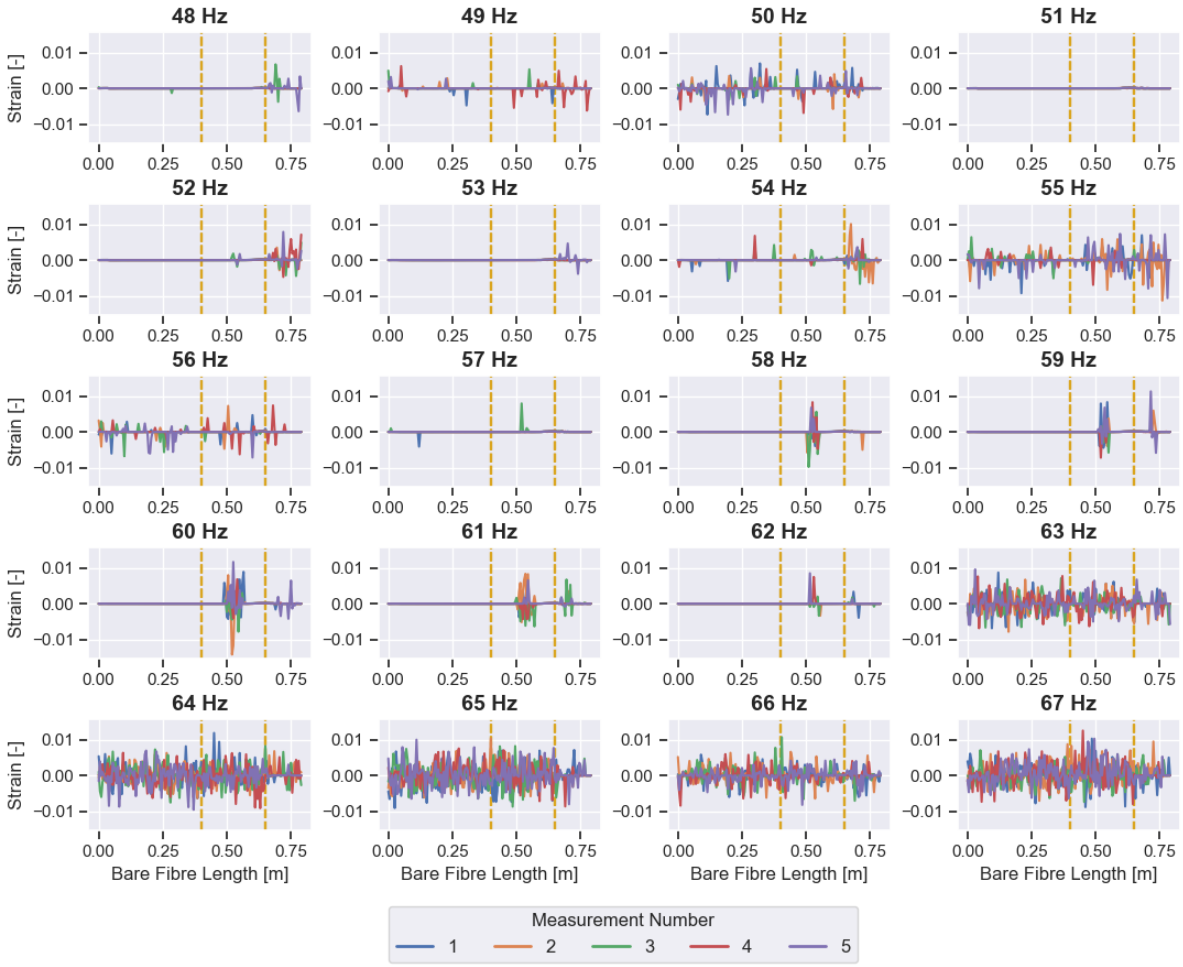

Figure A.2: Strain measurements gathered at 50% maximum volume. The vertical lines mark the section of the DOFS bonded to the composite beam.

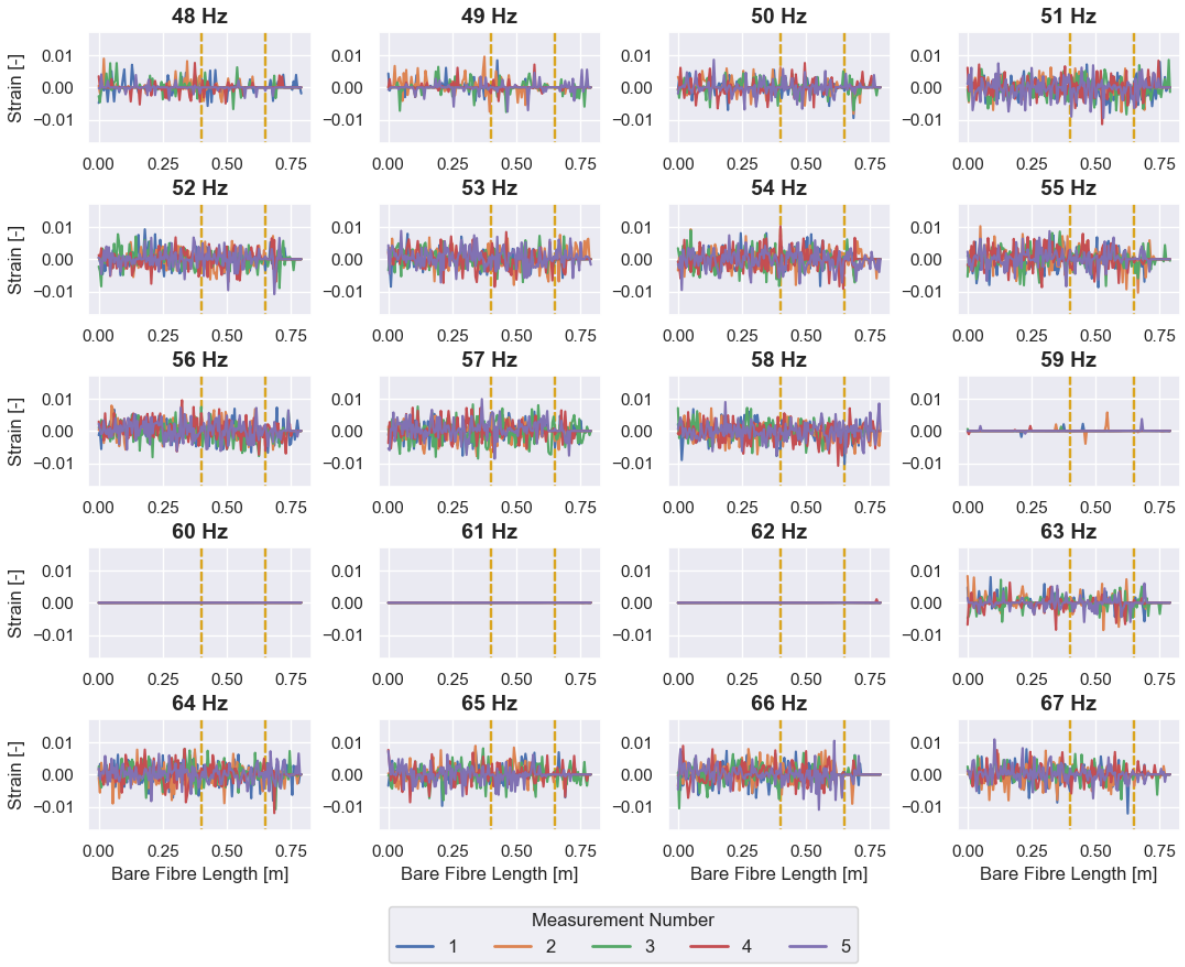

Figure A.3: Strain measurements gathered at 75% maximum volume. The vertical lines mark the section of the DOFS bonded to the composite beam.

Appendix B Risk Assessment

Sikkerhets- og kvalitetsgjennomgang av laboratorietester og verkstedsarbeid

Risk Assessment of Activities in the Laboratory and Workshop

NTNU

Rev. 10, 2020-Sep

ONLY VALID FOR DETAILED ACTIVITIES LISTED IN SECTION 5

1 Identifikasjon - *Identification*	**Dokumentnr. – *Document no.*:**	
Kundenavn – *N/A*	Prosjektnavn – *Project name* *Automatic detection of compromised sensors and data*	Projektnr. – *Project no.* *70443320*
Beskrivelse av arbeid – *Description of job* *Generating data from optical fiber sensors embedded in laminates*		Dato (fra -til) – *Date (from – to)* *06/09/2021-15/06/2022* *Updated 10/03/2022*

2 Projekt – *Team*			put in *NR* if not relevant
Prosjektleder og organisasjon – *Project manager and organisation (Student)*	Valeria Usenco	Ansvarlig for instrumentering – *Responsible for instrumentation.*	Valeria Usenco
Leiestedsansvarlig – *Laboratory responsible*	Ying Qian	Operatør – *Operator*	Valeria Usenco
Auditør for sikkerhets og kvalitetsgjennomgang – *Auditer for safety check*	Kaspar Lasn Ying Qian	Ansvarlig for styring av forsøk – *Responsible for running the experiment.*	Kaspar Lasn Valeria Usenco
Ansvarlig for eksperimentelt faglig innhold – *Responsible for experimental and scientific content(Veileder/Advisor)*	Kaspar Lasn	Ansvarlig for logging av forsøksdata – *Responsible for logging and storing experimental data*	Valeria Usenco
Ansvarlig for dimensjonering av last og trykkpåkjente komponenter – *Reponsible for dimensioning load bearing and pressurized components*	Valeria Usenco	Ansvarlig for montering av testrigg – *Responsible for building the rig*	Valeria Usenco

3 Viktig!! – *Important!!*	J: Ja – *Yes* / N: Nei - *No*
Er arbeidsordren signert? – *Is the work order signed?* *(only for external work)*	N/A
Har operatøren nødvendig kurs/trening i bruk av utstyret? - *Has the operator the required courses/training on the equipment?*	Yes
Har operatøren sikkerhetskurs? (påbudt) – *Has the operator followed the safety courses? (mandatory)*	Yes
Kan jobben gjøres alene? - *Can the work be done alone?*	Yes
- Dersom ja, er det med visse forbehold (for eksempel, må bruke alarm, ha avtale med noen som kommer innom med jevne mellomrom eller lignende). Dette må vurderes i Seksjon 5. *If yes, the work may have to be done under special conditions (e. g. must use the alarm, have agreement with somebody coming back periodically or similar).*	
Må en ekspert se på oppstart av eksperimentet? Does an expert have to check the start of the experiment?	Yes
- Dersom ja, hvem? *If yes, who?* Kaspar Lasn / Shaoquan Wang	

4.1 Sikkerhet – *Safety* (Testen medfører – *The test contains*)			J: Ja – *Yes* / N: Nei - *No*
Stor last – *Big loads*	No	Brannfare – *Danger of fire*	Yes
Tunge løft – *Heavy lifting*	No	Arbeid i høyden – *Working at heights*	No
Hengende last – *Hanging load*	No	Hydraulisk trykk – *Hydraulic pressure*	No
Gasstrykk – *Gas pressure*	No	Vanntrykk – *Water pressure*	No
Høy temperatur – *High temperature*	Yes	Lav Temperature – *Low temperature*	Yes
Deler i høy hastighet – *Parts at high velocity*	No	Farlige kjemikalier – *Dangerous chemicals*	Yes
Sprutakselerasjon ved brudd – *Sudden acceleration at fracture/failure*	No	Forspente komponenter – *Pre-tensioned components*	No
Farlig støv – *Dangerous dust*	No	Kraftig støy – *Severe noise*	No
Klemfare – *Danger of pinching*	Yes	Roterende deler – *Rotating parts*	No

4.2 Påkrevet verneustyr – *Required safety equipment*			J: Ja – *Yes* / N: Nei - *No*
Briller (påbudt) – *Glasses (mandatory)*	Yes	Vernesko – *Safety shoes*	Yes
Hjelm – *Helmet*	No	Hansker – *Gloves*	Yes
Skjerm – *Screen*	No	Visir – *Visir*	No
Hørselsvern – *Ear protection*	Yes	Løfteredskap – *Lifting equipment*	No
Yrkessele, fallsele, etc. – *Harness ropes, other measures to prevent falling down.*	No	Full vernedress – Hazard suit	No

Sikkerhets- og kvalitetsgjennomgang av laboratorietester og verkstedsarbeid

NTNU
Perleporten

5.1 Beskrivelse av aktivitet – *Description of the activity (see Appendix)*

Vurdering skal være basert på en skriftlig prosedyre for bruk av maskinen. I enkelte tilfeller kan prosedyre bli beskrevet direkte i tabellen nedenfor.

The evaluation shall be based on a written operating procedure for the machine. For simple cases the procedure can be directly described in the tables below.

Nr.	Beskrivelse av aktivitet *– Description of activity*	Fare – *Danger*	Lov, forskrift o.l. *– Legal requirements*	Prosedyre nr. *– Procedure no.*	Sannsynlighet *– Probability*	Konsekvens *–Consequence*	Risiko *– Risk*
1	Use of laser	Damage to eye			2	B	B2
2	Burning off fiber coating	Fire / burn injury			1	C	C1
3	Cutting optical fiber	Cutting injury			2	A	A2
4	Sharing lab with others	Covid-19			3	C	C3
5	Using wire stripper	Pinching			2	A	A2
6	Using OBR machine	Breaking it			1	D	D1
7	Using simple sensor system	Electricity issues			1	B	B1
8	Handling epoxy and hardener	Inhaling fumes or eye/skin irritation from exposure			2	D	D2
9	Handling epoxy and hardener	Spillage			4	B	B4
10	Using acetone for cleaning	Inhaling/eye irritation			2	C	C2
11	Acoustic testing	Excessive noise			2	C	C2

5.2 Korrigerende Tiltak – *Corrective Actions*

Nr.	Korrigerende tiltak – Corrective action	Sannsynlighet *– Probability*	Konsekvens *– Consequence*	Risiko *– Risk*	Utført dato *– Date of action*
2	Clear away flammable materials when using butane torch, do not touch hot parts	1	B	B1	
4	Social distancing and use of medical mask	1	C	C1	
6	Use clean hands and equipment, fence in equipment, use proper procedures as demoed	1	B	B1	
8	Ensure there is good ventilation, use gloves and do not touch eyes	2	B	B2	
9	Walk carefully when carrying epoxy mix, clean up spillage as soon as possible	2	A	A2	
10	Ensure there is good ventilation, use gloves and do not touch eyes	1	A	A1	
11	Use ear protection, perform experiment away from others	2	A	A2	

Sikkerhets og kvalitetsgjennomgang av laboratorietester og verkstedsarbeid

NTNU
Perleporten

5.3 Feilkilder – *Reasons for mistakes/errors*

Er følgende feilkilder vurdert? –Is the following considered? J: Ja – *Yes* / N: Nei – *No* / *NR: not relevant*

Tap av strøm – *Loss of electricity*	Yes	Overspenning – *Voltage surge*	NR
Elektromagnetisk støy or Jordfeil – *Electromagnetic noise – Electrical earth failure*	NR	Manglende aggregatkapasitet av hydraulikk – *Insufficient power of the machine*	NR
Klimakontroll i rom – *Climate control in the room (temp, humidity, etc.)*	Yes	Vannsprut – *Water jet*	NR
Ustabilt trykk av hydraulikk/kraft – *Unstable pressure or hydraulic force*	NR	Tilfeldig avbrudd av hydraulikk/kraft – *Unintended interruption of power supply*	NR
Last-/ forskyvnings grenser etablert ? – *Are load and displacement limits established?*	NR	Lekkasjer (slanger/koblinger, etc.) – *Leakage of pipes, hoses, joints, etc.*	Yes
Mulige påvirkninger fra andre aktiviteter – *Possible interference from other activities*	Yes	Mulige påvirkninger på andre aktiviteter – *Possible interference towards other activities*	Yes
Problemer med datalogging og lagring – *Troubles in acquisition and storage*	Yes	Brann i laboratoriet – *Fire in the laboratory*	Yes

6 Kalibreringsstatus for utstyr – *Calibration of equipment*

(ex: load cell, extensometer, pressure transducer, etc)

I.D.	Utstyr – *Equipment*	Gyldig til (dato) – *Valid until (date)*
1	Calibration according of equipment according to MTP lab	15/06/2022

7 Sporbarhet – *Tracebility*

Eksisterer – Is there J: Ja – *Yes* / N: Nei – *No* / *NR: not relevant*

Er alle prøvematerialene kjente og identifiserbare? – *Are all experimental materials known and traceable?*	Yes
Eksisterer det en plan for markering av alle prøvene? – *Is there a plan for marking all specimens?*	Yes
Er dataloggingsutstyret identifisert? – *Is the data acquisition equipment identified?*	Yes
Er originaldata lagret uten modifikasjon? – *Are the original data stored safely without modification?*	Yes
Eksisterer det en backup-prosedyre? – *Is there a back-up procedure for the data (hard disk crash)?*	Yes
Eksisterer det en plan for lagring av prøvestykker etter testing? – *Is there a plan for storing samples after testing?*	Yes
Eksisterer en plan for avhending av gamle prøvestykker? – *Is there a plan for disposing of old samples?*	Yes

8 Kommentarer – *Comments*

9 Signaturer – *Signatures)*

a pdf copy of the signed document shall be sent to Andreas.Echtermeyer@ntnu.no

Godkjent (dato/sign) – Approved (date/signature ***a paper copy shall be available in the composite lab***

Prosjektleder – *Project leader*	Verifikatør – *Verifier*	Godkjent – *Approved by*	Godkjent – *Approved by*
(Student) *Valeria Usenco*	(Veileder - *Advisor)* *Kaspar Lasn*	(*Romansvarlig* - Room responsible *)* *Andreas Echtemeyer*	(Labor sjef - *Laboratory Leader)* Ying Qian

Sannsynlighet vurderes etter følgende kriterier:
Probability shall be evaluated using the following criteria:

Svært liten Very unlikely **1**	**Liten** Unlikely **2**	**Middels** Probable **3**	**Stor** Very Probable **4**	**Svært stor** Nearly certain **5**
1 gang/50 år eller sjeldnere *– Once per 50 years or less*	1 gang/10 år eller sjeldnere *– Once per 10 years or less*	1 gang/år eller sjeldnere *– Once a year or less*	1 gang/måned eller sjeldnere *– Once a month or less*	Skjer ukentlig *– Once a week*

Konsekvens vurderes etter følgende kriterier:
Consequence shall be evaluated using the following criteria:

Gradering *– Grading*	**Menneske** *– Human*	**Ytre miljø, Vann, jord og luft** *– Environment*	**Øk/materiell** *– Financial/Material*	**Omdømme** *– Reputation*
E **Svært Alvorlig** ***– Very critical***	Død – Death	Svært langvarig og ikke reversibel skade *– Very prolonged, non-reversible damage*	Drifts- eller aktivitetsstans >1 år. *– Shutdown of work >1 year.*	Troverdighet og respekt betydelig og varig svekket *– Trustworthiness and respect are severely reduced for a long time.*
D **Alvorlig** ***– Critical***	Alvorlig personskade. Mulig uførhet. *– May produce fatality/ies*	Langvarig skade. Lang restitusjonstid *– Prolonged damage. Long recovery time.*	Driftsstans > ½ år Aktivitetsstans i opp til 1 år *– Shutdown of work 0,5-1 year.*	Troverdighet og respekt betydelig svekket *– Trustworthiness and respect are severely reduced.*
C **Moderat** ***– Dangerous***	Alvorlig personskade. *– Permanent injury, may produce serious health damage/sickness*	Mindre skade og lang restitusjonstid *– Minor damage. Long recovery time*	Drifts- eller aktivitetsstans < 1 mnd *– Shutdown of work < 1 month.*	Troverdighet og respekt svekket *– Troverdighet og respekt svekket.*
B **Liten** ***– Relatively safe***	Skade som krever medisinsk behandling *– Injury that requires medical treatment*	Mindre skade og kort restitusjonstid *– Minor damage. Short recovery time*	Drifts- eller aktivitetsstans < 1uke *– Shutdown of work < 1 week.*	Negativ påvirkning på troverdighet og respekt *– Negative influence on trustworthiness and respect.*
A **Siker** **- Safe**	Injury that requires first aid	Insignificant damage. Short recovery time	Shutdown of work < 1day	

Risikoverdi = Sannsynlighet X Konsekvenser
Beregn risikoverdi for menneske. IPM vurderer selv om de i tillegg beregner risikoverdi for ytre miljø, økonomie/ material og omdømme. I så fall beregnes disse hver for seg.

Risk = Probability X Consequence
Calculate risk level for humans. IPM shall evaluate itself if it shall calculate in addition risk for the environment, economic/material and reputation. If so, the risks shall be calculated separately.

Risikomatrisen

Risk Matrix

I risikomatrisen er ulike grader av risiko merket med rød, gul eller grønn:

Rød: Uakseptabel risiko. Tiltak skal gjennomføres for å redusere riskoen.

Gul: Vurderingsområde. Tiltak skal vurderes.

Grønn: Akseptabel risiko. Tiltak kan vurderes ut fra andre hensyn.

Når risikoverdien havner på rødt felt, skal altså enheten gjennomføre tiltak for å redusere risikoen. Etter at tiltak er iverksatt, skal dere foreta ny risikovurdering for å se om risikoen har sunket til akseptabelt nivå.

For å få oversikt over samlet risiko: Skriv risikoverdi og aktivitetens IDnr. i risikomatrise (docx) / risikomatrise (odt). Eksempel: Aktivitet med IDnr. 1 har fått risikoverdi 3D. I felt 3D i risikomatrisen skriver du IDnr. 1. Gjør likedan for alle aktiviteter som har fått en risikoverdi. En annen måte å skaffe oversikt på, er å fargelegge feltet med risikoverdien i skjemaet for risikovurdering. Dette tydeliggjør og gir samlet oversikt over riskoforholdene. Ledelse og brukere får slik et godt bilde av risikoforhold og hva som må prioriteres.

In the risk matrix different degrees of risk are marked with red, yellow or green;

Red: Unacceptable risk. Measures shall be taken to reduce the risk.

Yellow: Assessment Area . Measures to be considered.

Green: Acceptable risk. Measures can be evaluated based on other considerations.

When a risk value is red, the unit shall implement measures to reduce risk. After the action is taken, you will make a new risk assessment to see if the risk has decreased to acceptable levels.

To get an overview of the overall risk: Write the risk value and the task ID no . the risk matrix (docx) / risk matrix (odt) . Example : Activity with ID no . 1 has been risk value 3D. In the field of 3D risk matrix type ID no . 1 Do the same for all activities that have been a risk . Another way to get an overview is to color the field of risk value in the form of risk assessment . This clarifies and gives overview of the risk factors . Management and users get such a good picture of the risks and what needs to be prioritized.

KONSEKVENS						
	Svært alvorlig	E1	E2	E3	E4	E5
	Alvorlig	D1	D2	D3	D4	D5
	Moderat	C1	C2	C3	C4	C5
	Liten	B1	B2	B3	B4	B5
	Svært liten	A1	A2	A3	A4	A5
		Svært liten	Liten	Middels	Stor	Svært stor
		SANNSYNLIGHET				

Prinsipp over akseptkriterium. Forklaring av fargene som er brukt i risikomatrisen.

Farge		Beskrivelse
Rød		Uakseptabel risiko. Tiltak skal gjennomføres for å redusere risikoen.
Gul		Vurderingsområde. Tiltak skal vurderes.
Grønn		Akseptabel risiko. Tiltak kan vurderes ut fra andre hensyn.

Til Kolonnen "Korrigerende Tiltak":

Tiltak kan påvirke både sannsynlighet og konsekvens. Prioriter tiltak som kan forhindre at hendelsen inntreffer, dvs sannsynlighetsreduserende tiltak foran skjerpende beredskap, dvs konsekvensreduserende tiltak.

For Column "Corrective Actions"

Corrections can influence both probability and consequence. Prioritize actions that can prevent an event from happening.

Oppfølging:

Tiltak fra risikovurderingen skal følges opp gjennom en handlingsplan med ansvarlige personer og tidsfrister.

Follow Up

Actions from the risk evaluation shall be followed through by an action plan with responsible persons and time limits.

Etterarbeid #

- Gå gjennom aktiviteten/prosessen på nytt.
- Foreta eventuell ny befaring av aktiviteten/prosessen for enten a) å få bekreftet at risikoverdiene er akseptable eller b) for å justere risikoverdiene.
- Gå gjennom, vurder og prioriter tiltak for å forebygge uønskede hendelser. Først skal dere prioritere tiltak som reduserer sannsynlighet for risiko. Dernest skal dere ta for dere tiltak som reduserer risiko for konsekvenser.
- Tiltakene skal føres inn i handlingsplanen. Skriv fristen for å gjennomføre tiltaket (dato, ikke tidsrom) og navn på den / de som har ansvar for tiltakene.
- Foreta helhetsvurdering for å avgjøre om det nå er akseptabel risiko.
- Ferdig risikovurdering danner grunnlag for å utarbeide lokale retningslinjer og HMS-dokumenter, opplæring og valg av sikkerhetsutstyr.
- Ferdig risikovurdering og eventuelle nye retningslinjer gjøres kjent/tilgjengelig for alle involverte.
- Sett eventuelt opp kostnadsoverslag over planlagte tiltak.

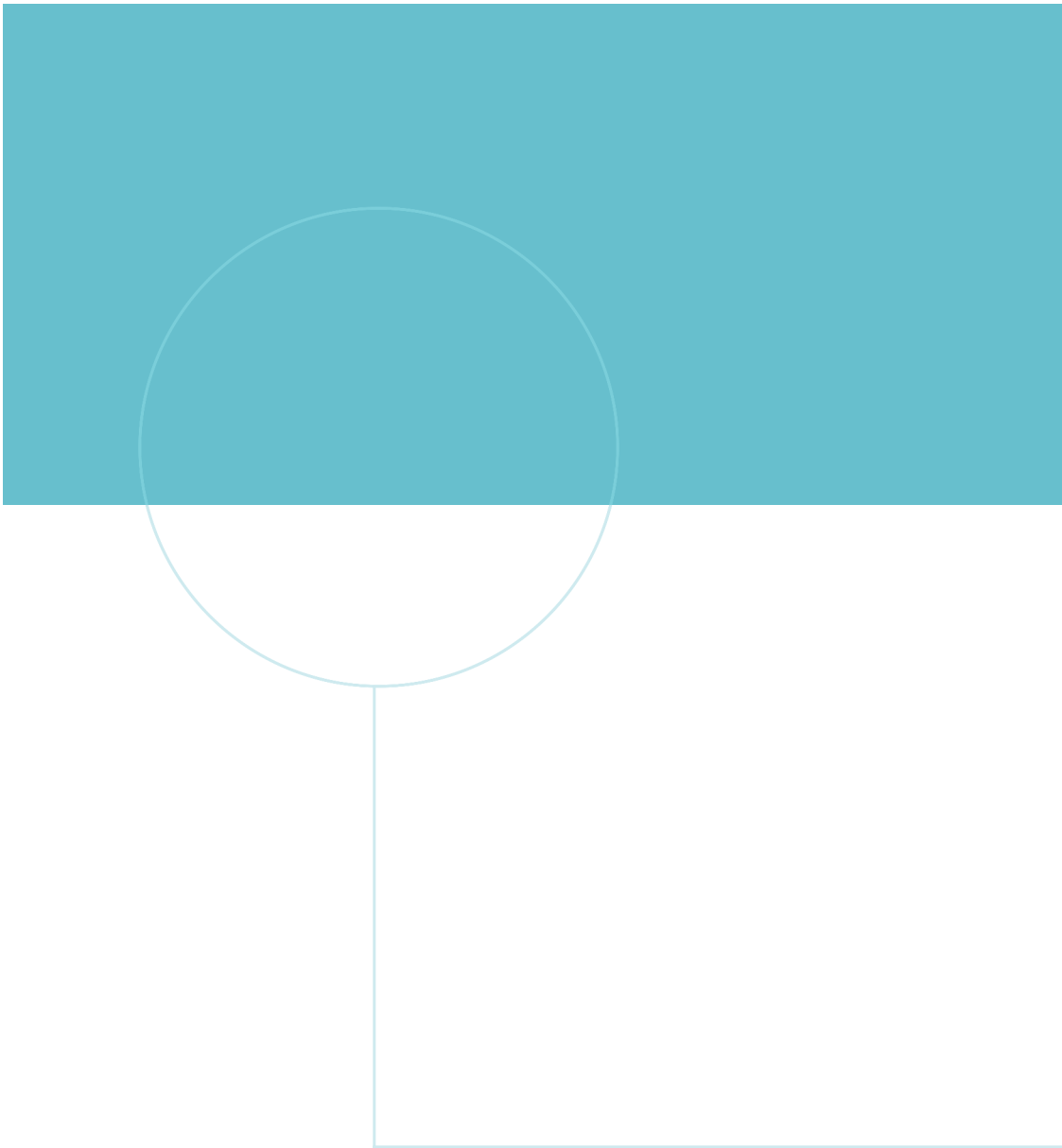

NTNU

Norwegian University of
Science and Technology